J. Electrochem. Sci. Eng. **00(0)** (2022) 000-000; http://dx.doi.org/10.5599/jese.1470

Open Access : : ISSN 1847-9286
www.jESE-online.org

Review paper

Brief review on carbon derivatives based ternary metal oxide composite electrode materials for lithium-ion batteries

Veerabhadrachar Pavitra[1,2], Isha Soni[3], Beekanahalli Mokshanatha Praveen[1] and Ganganagappa Nagaraju[2,✉]

[1]*Department of Nanotechnology, College of Engineering and Technology, Srinivas University, Mukka, Mangaluru-574146, Karnataka, India*
[2]*Energy Materials Research Laboratory, Department of Chemistry, Siddaganga Institute of Technology (Affiliated to VTU, Belagavi), Tumakuru-572103, India*
[3]*Laboratory of Quantum Electrochemistry School of Advanced Chemical Sciences, Shoolini University, Bajhol, Solan, Himachal Pradesh 173229, India*

Corresponding author: ✉bm.praveen@yahoo.co.in

Received: July 26, 2022; Accepted: November 14, 2022; Published: December 8 2022

Abstract

Revolutionized lithium-ion batteries (LIB) have taken a very important role in our day today life by powering all sorts of electric devices. The selection of electrode materials is very important, which impacts the electrochemical performance of LIBs. Advancements in the electrode materials and synthesis procedure greatly influence the electrochemical performance. This review discusses the carbon derivatives based ternary composite as electrode materials. A detailed explanation of the ternary electrode materials synthesis and spectroscopic, microscopic and electrochemical analysis of LIBs has been carried out in this study. Ternary composites are composed of highly conducting carbon derivatives, which are incorporated with SnO_2/ZnO/MoO_3/SiO_x and additionally any one metal oxide. Carbon derivatives-based ternary metal oxide composites can exhibit enhanced electrochemical results based on their heterostructures. The availability of more active sites contributes the reversible topotactic reactions during the charging-discharging process due to the porosity and other unique structures of different dimensions of the electrode materials. Concepts and strategies can extend the focus on developing the ternary metal oxides for high-performance LIBs.

Keywords

Nanoparticles; SnO_2; ZnO; MoO_3; SiO_x, ternary composite; LIBs

Introduction

The development of high energy storage materials is a global challenge to combat the rise in fuel prices and environmental problems brought on by the rapid depletion of non-renewable and intermittent renewable energy sources like wind, solar, geothermal biomass, tidal and wind [1,2].

Electrochemical energy storage systems exhibit zero emission, which is necessary to fulfill the large energy demands worldwide and to drive electric gadgets and electric vehicles (EVs) [3]. Large-scale sustainable and portable electrical devices' main consideration is lithium-ion batteries (LIBs) because of their high charge storage capacity, power and energy densities, and low self-discharge rate [4]. The operating principle of LIBs is based on the movement of Li^+ ions between the electrodes. During discharge, lithium ions move from the anode to the cathode and the reverse mechanism occurs during the charging process, *i.e.* Li^+ ions move from the cathode to the anode. Electrons move through an external circuit. Since the intercalation of lithium takes place on both electrodes, electrode materials play a vital role in improving electrochemical performance for facilitating topotactic activity [5]. Developing different electrode materials for LIBs has gained a lot of attention. A schematic representation of the Li-ion battery (LIBs) is shown in Figure 1**.**

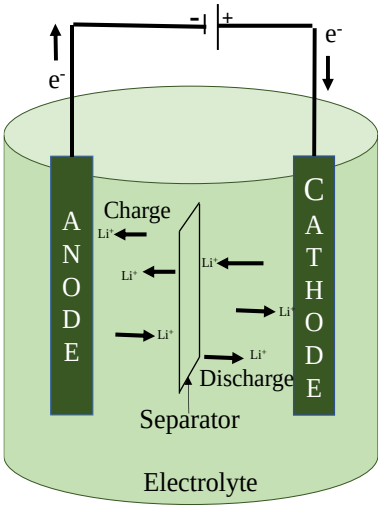

Figure 1. *Schematic representation of the Li-ion battery operation*

Metal oxides (MOs) have received increased attention and are being exploited in energy storage applications due to their simple synthesis procedures and potential to deliver superior electrochemical performance. Graphite exhibits a lower gravimetric capacity, *i.e.* 372 mAh g^{-1}, than metallic lithium because it cannot increase the Li content beyond LiC_6 [6]. Additionally, graphite operates at a decreased voltage compared to metallic lithium anode. On the other hand, numerous structural geometries with electronic structures highlight the metallic, semiconductor, or insulator properties of MOs electrode materials. MOs are employed in a wide range of applications in the technological realm. Due to the size, surface area, and density of their particles, oxides at the nanoscale size exhibit special and distinctive physical and chemical properties. Particle size affects how lattice symmetry and cell characteristics are changed. Low surface free energy is related to thermodynamic stability and is attained by metal oxides in the nanoscale size. Numerous MO nanoparticles (NPs) have been thoroughly researched in terms of their cost- and abundance-benefits as hosts for ion insertion [7-9]. In the carbon derivatives-based ternary metal oxide (CDTMOs), electron mobility will be greatly enhanced through the entire surface. Synergistic effects among the materials help to overcome the individual MOs drawbacks and impacts in increasing the overall electrochemical performance. Functionalization of the carbonaceous materials with the MO NPs greatly enhances the electrochemical performance of LIBs. CDTMOs also act as a buffer matrix to reduce the capacity fading issues that occur through volume expansion. Besides, materials undergo less aggregation and enhance ionic conductivity [10-14].

Usually, single metal oxides suffer from large volume expansion, which leads to poor electrochemical performance. Literature suggested that the designing of electrodes with more than one

metal oxide and carbon materials could enhance the electrochemical activity. Li^+ insertion-extraction takes place in both the metal oxides. It enhances the kinetics of redox reactions and electrical conductivity [15]. Usually, SnO_2 and ZnO undergo alloy reactions with Li metal and form Li_xSnO_y/ LiCuO phases, or directly, they may undergo a partial conversion reaction. Some papers mentioned that SnO_2 undergoes irreversible conversion and ZnO undergoes reversible conversion reactions [16]. Materials that undergo conversions and alloying-dealloying reaction mechanisms deliver superior electrochemical performance than those that involve only one reaction [17]. Carbon materials act as buffer matrices and help to avoid volume expansion, while MO composites protect the active materials from aggregation. Binary composites are more remarkable than ternary composites.

Here in this review, we will provide a comprehensive review of carbon derivatives-based ternary metal oxide compounds for LIBs. It includes a detailed discussion of the electrode materials synthesis procedure and the spectroscopic as well as microscopic analysis of CDTMOs. Among the various available metal oxides, we have considered mainly carbon derivatives incorporated to SnO_2, ZnO, MoO_3, SiO_x and other MOs synthesis procedure, morphologies, and their electrochemical performance for LIBs from various literature.

Synthesis of carbon derivatives based ternary metal oxide (CDTMOs) composites

Synthesis of nanomaterials is broadly categorized into top-down and bottom-up approaches, Figure 2. The top-down method uses chemical, mechanical, or other energy sources for the synthesis. Electron beam lithography [18], Aerosol spray [19], Gas-phase condensation [20], and Ball milling [21] are some of the techniques that fall under the top-down approach. The bottom-up synthesis strategy of nanomaterials derived from atoms or molecules includes Hydrothermal [22], Co-precipitation [23], Ultrasonication [24], Sol-gel [25], Electrodeposition [26] and Combustion [27] methods.

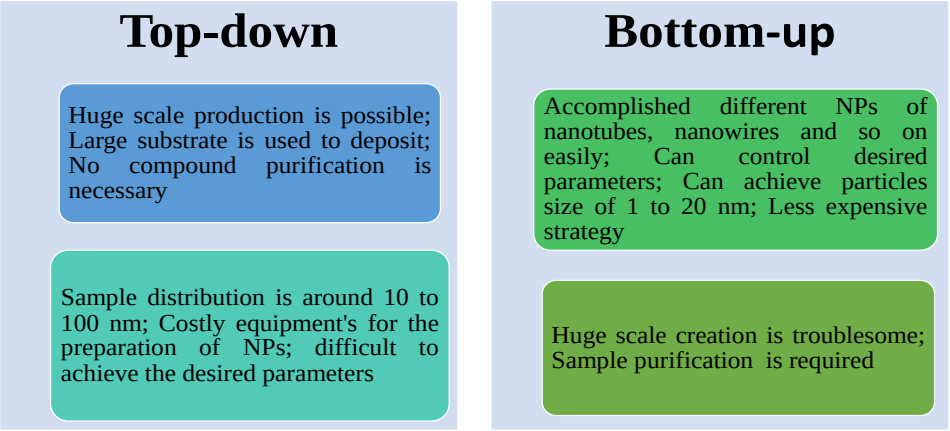

Figure 2. *Advantages and disadvantages of top-down and bottom-up approaches*

The bottom-up approach is preferable for electrode materials preparation because it can achieve uniform chemical composition and defect-free nanostructures. The bottom-up methods are cost-effective, less time-consuming, and simple procedures for material preparation. To achieve the superior electrochemical performance of LIBs, electrode materials of high surface area and unique morphology are very important. Varying the different experimental parameters, such as operating temperature and duration, while synthesizing the electrode materials, it is possible to achieve the desired particles' size, shape and structure. Various unique structures of different dimensions of 2D and 3D will become more conductive and facilitates ion transportation with a large surface area by creating more active sites [28].

Carbonaceous materials

CDTMOs can be prepared by in-situ wet chemical bottom-up routes or through ex-situ. *i.e.* mechanical mixing of the prepared individual metal oxide compounds [29]. Carbon derivatives can exhibit splendid electrochemical activity because of their higher conductivity and surface area [30]. By combining different metal oxides, it is possible to overcome the individual metal oxide drawbacks due to synergistic effects. Each individual metal oxide has a different role by possessing the multiple oxidation states in the composite, which makes the feasible topotactic redox reactions in the LIBs easier. This way, they greatly enhance the rate performance, cyclic stability and storage capacity of LIBs because they have very good conductivity and high surface area of carbonaceous materials.

This review discusses the ternary composites composed of two MOs and a carbon derivative. Carbon derivatives include GO (graphene oxide), rGO (reduced graphene oxide)/ graphene, CNT (carbon nano tubes), SWCNT (single-walled carbon nano tubes), MWCNT (multi-walled carbon nano tubes) [31-35].

The impressive adsorption capacity of metal ions can be accomplished by the high surface area of GO, this acts as a potential sink of electrons by providing great electron mobility. The hydrophilic and dispersible nature of GO can be varied by the availability of vast number of epoxides and OH functional groups. Hummer's method is the standard procedure for the preparation of GO using sulfuric acid and potassium permanganate. Some sulfur impurities are often found when the preparation is performed with organosulfate groups. Due to this demerit, research was extended to add some modifications. In the modified Hummer's method [36], double bonds of GO are unlikely to persist in strong oxidizing conditions.

Graphene/rGO provide a huge surface area of 2600 m^2/g compared to GO, *i.e.,* 890 $m^2\ g^{-1}$ [37]. Therefore, rGO facilitates a very good topotactic activity of Li ions during redox reactions. rGO is a 2D monoatomic layer of GO, which is composed of hexagonal structures of sp^2 hybridized carbon atoms. The rGO can be obtained by exfoliating and reducing the GO of 0.142 nm interlayer distance. It acts as a matrix for enabling the electrons and ions to migrate into the active sites. It could greatly increase the energy density, relieve the strain, and avoid particle agglomeration during redox reactions in LIBs. rGO also has high thermal conductivity and is stable for longer periods [38,39]. There are several methods to prepare rGO. Green extracts are good reducing agents can be used for the reduction of GO. Commonly used inorganic reducing agents are ascorbic acid, oxalic acid, sodium borohydride, *etc* [40].

Carbon nanotubes (CNTs) provide higher surface area, high conductivity, provides good ion transport channels and can restrain the π-π interaction of graphene. Therefore, CNTs act as graphene modifiers. CNTs and graphene have almost comparable conductivities, but CNTs undergo more controlled diffusion of Li ions than graphene during charging-discharging process. Therefore, CNTs provide superior ionic transport channels [41]. CNTs greatly alter the surface characteristics of electrode materials compared to graphene and avoid the agglomeration of the active materials during the topotactic activity of LIBs. This enables higher initial discharge capacity and cyclic rate performance in the LIBs. CNT is also a good additive for the electrode material due to its excellent electrical conductivity, large surface area and high aspect ratio [42]. CNTs are prepared by many methods, such as chemical vapor deposition (CVD) [43], arc discharge [44], laser ablation [45], *etc*.

Despite the many crucial advantages, such as increasing electronic conductivity and reducing pulverization by adding carbon derivatives, there will be a compromise between capacity and cyclic life because carbon is hardly active and low density of the carbon additives, results a poor volumetric and gravimetric energy densities. The battery electrode's faradaic contribution will also be diminished. Therefore, it is desirable to tune the carbon additives content in the final compound [46].

Different synthesizing methods

Sonochemical method

The sonochemical method is very effective for obtaining the uniform distribution of the particles through ultrasonic radiation. In this method, the precursor's solution is sonicated to carry out the ultrasonication. During the reaction, the atoms diffuse into the bubbles by ultrasonic radiation of 20 kHz-10 MHz and undergo mechanical agitation in liquid solution. Nucleation and diffusion of the molecules, as in terms cause the breakage of chemical bonds, takes place in the sonicator [47]. Potle *et al.* [48] sonochemically prepared the ternary composite of rGO-ZnO-TiO_2. They began by combining GO, titanium isopropoxide, and zinc acetate in NaOH solution and sonicated for 60 min. The reaction mixture was washed and dried to obtain the final ternary composite rGO-ZnO-TiO_2. Raj *et al.* [49] prepared NZnO–Mn_2O_3@rGO composite by the sonochemical method using manganese oxide (Mn_2O_3) and nitrogen-doped zinc oxide (NZnO). Equimolar ratios of the precursors were homogeneously ultrasonicated for 30 min and then stirred for 1 h vigorously. They were finally calcined at 750 °C for 3 h. Asgar *et al.* [50] fabricated a hybrid nanocomposite of ZnO-CuO-rGO through the sonochemical method. GO suspension was dissolved in Zn $(NO_3)_2$ and Cu (II) sulfate precursors by maintaining pH 11 of the mixture by adding 1 M KOH. The final particles were heat treated at 200 °C in the air for 2 h. T. Shinde *et al.* [51] prepared graphene- Ce-TiO_2 and graphene-Fe-TiO_2 nanocomposites through a sonochemical route using titanium isopropoxide, cerium nitrate, NaOH and GO in sonicator and calcined at 300 °C for 3 h for graphene- Ce-TiO_2 preparation and titanium isopropoxide, ferric nitrate, NaOH and GO sonicated for 30 min calcined at 300 °C for 3 h to obtain graphene-Fe-TiO_2 ternary composite. Table 1. explains the CDTMOs composites prepared sonochemically.

Table 1. *Sonochemical synthesis of ternary composites*

No	Ternary composites	Reaction time, min	Advantages	Ref.
1	rGO-ZnO-TiO_2	60	Application of ultrasound impacts the uniform dispersion of ZnO and TiO_2 NPs on graphene sheets	[48]
2	NZnO- Mn_2O_3@rGO	30	High acoustic cavitation significantly reduces the attraction force between individual particles, leading to the formation uniform sized particles	[49]
3	ZnO-CuO-rGO	60	Prevention of aggregation	[50]
4	rGO-Ce-TiO_2	60	High surface area	[51]
5	rGO-Fe-TiO_2	30	Uniform dispersion of particles	[51]

Combustion method

The combustion method is a single-step technique and an easy procedure for the preparation of metal oxide NPs. This method is cost-effective, less time-consuming and helps with the creation of porosity in the structure. Usually, the combustion method prefers the bulk-scale production of NPs. The combustion method involves generating the NPs by applying the appropriate temperature to the specific quantity of oxidizer and fuel for the exothermic reactions. Nowadays, the preparation of metal oxides using green fuels is also trending [52]. Kumar *et al.* [53] synthesized GO-$CuFe_2O_4$-ZnO ternary nanocomposite by solution combustion method. Sonicated GO, copper nitrate (0.0991 g), iron (III) nitrate (0.02751 g) and zinc nitrate (0.0048 g) solution was kept in an electric jacket at a temperature of 300 °C to remove solvents until the combustion process and calcined to 350 °C for 12 h to obtain the final product. Rotte *et al.* [54] synthesized MgO and NiO decorated graphene composite through rudimentary combustion of ball-milled precursors. In this, Mg metal turnings (1 g), NiO (0.5 g) powder samples were mixed using ball milling with a 1:5 ratio. The mixed blend of NiO and Mg was combusted

in the presence of dry ice (solid CO_2). Rai *et al.* [55] have synthesized $MgFe_2O_4$/graphene ternary nanocomposite by the auto-combustion method. In the synthesis, the precursors of magnesium nitrate hexahydrate and iron(III) nitrate nonahydrate were of 1:2 ratio and urea as fuel along with the reduced graphene nanosheets in hot plate magnetic stirrer at 350 °C. They were finally annealed at 600 °C for 5 h in an N_2 atmosphere for the formation of $MgFe_2O_4$/graphene nanocomposite. Kang *et al.* [56] synthesized cobalt-nickel oxides with CNTs (Co/Ni/CNT) nanocomposite through one step solution combustion method using Co $(NO_3)_2{\cdot}6H_2O$, Ni $(NO_3)_2{\cdot}6H_2O$, citric acid and CNTs. Table 2. explains the CDTMOs composites prepared via the combustion method.

Table 2. *Combustion synthesis of ternary composites*

No	Ternary composites	Operating conditions	Advantages	Ref.
1	GO-$CuFe_2O_4$-ZnO	350 °C, 12 h	Nanoball interlinked structure over GO sheet	[53]
2	MgO- NiO / graphene	Dry ice (solid CO_2) 12 h at 100 °C	Wavy few-layered graphene	[54]
3	Mg Fe_2O_4 / graphene	600 °C for 5 h in N_2 atmosphere	Strong interfacial interaction between Mg Fe_2O_4 NPs and rGO	[55]
4	Co-Ni oxides / CNTs	300 °C, 30 min	Scalable	[56]

Hydrothermal route

The hydrothermal method has been considered for preparing the desired shape and sized NPs. Teflon-lined air-tight autoclave acts as a hydrothermal bomb to maintain the pressure. The hydrothermal method offers a simple, low-cost procedure and is conducted with easily available raw materials. In the solvothermal method, different solvents with different physical and chemical characteristics can affect the solubility, reactivity, and diffusion behavior of the reactants; in particular, the solvent's polarity and coordinating capability can affect the final product's shape and crystallization nature. The ionic liquid is employed as a co-solvent with water or an organic solvent in the iono-thermal process, which also involves heat treatment [57,58]. Botsa *et al.* [59] synthesized SnO_2-Fe_2O_3-rGO ternary composite through the hydrothermal method. Firstly, tin chloride (2 mmol), NaOH (0.1 mmol) was transferred into an autoclave at 190 °C for 22 h. 0.01 M of iron nitrate, 50 mL of ethanol, 0.5 g of SnO_2 powder were and with an appropriate amount of GO placed on a hot plate at 70 °C for 10 h for the ternary composite preparation and finally calcined at 300 °C for 6 h. M. Amarnath *et al.* [60] have prepared rGO/Mn_3O_4/V_2O_5 ternary composite by hydrothermal route. In the beginning, Mn_3O_4 and V_2O_5 were prepared by hydrothermal route. Preparation of rGO/Mn_3O_4 begins with the preparation of GO, then ultrasonically mixed with hydrazine hydrate (10 mL) to reduce GO to rGO solution and $KMnO_4$ (0.1 M), and all together transferred into an autoclave (100 mL) at 180 °C for 24 h. For V_2O_5 preparation, $NaVO_3$ (1 g) and $KMnO_4$ were used for ultrasonication. Then both solutions were transferred into an autoclave at 180 °C for 24 h. Chung *et al.* [61] prepared CuO/RuO_2/MWCNTs hydrothermally using cupric acetate monohydrate and ruthenium chloride hydrate in N-methylpyrrolidone as a surfactant, sonicated MWCNT and NaOH were transferred to autoclave under 180 °C for 12 h. Kumar *et al.* [62] synthesized CeO_2-SnO_2/rGO by low-temperature hydrothermal method. Sonicated GO, $Ce(SO_4)_2{\cdot}4H_2O$ (0.08 M) and $SnCl_2{\cdot}2H_2O$ (0.02 M), NaOH (2 M) were transferred into the autoclave at 150 °C for 2 h. Wu *et al.* [63] fabricated the SnO_2-Fe_2O_3/SWCNTs nanocomposite through the hydrothermal method using $SnCl_4{\cdot}H_2O$ (0.2 mmol), $Fe(NO_3)_3{\cdot}9H_2O$ (0.25 mmol) and sonicated SWCNTs in phthalic acid (0.2 mmol) was added to the hydrothermal bomb for the reaction to occur at 180 °C for 48 h. Huang *et al.* [64] prepared SnO_2/NiO/graphene ternary composite via hydrothermal route using nickel nitrate (0.005 mol), sodium dodecyl sulfate (0.05 mol), tin chloride (0.01 mol) with GO in ethanol transferred into autoclave maintained at 200 °C for 18 h and calcined at 600 °C for 2 h.

Zhao *et al.* [65] developed SnO_2-CuO/graphene composite synthesized via a hydrothermal route. CuO/graphene nanocomposite prepared using copper acetate, cetyltrimethylammonium bromide (CTAB) as a cationic surfactant, and ultrasonicated graphene nanosheets in a hydrothermal bomb at 120-150 °C for 12 h. Obtained CuO/graphene, tin chloride, NaOH, NaCl, again transferred into an autoclave for the hydrothermal reaction at 80 °C for 24 h. Xiaoli *et al.* [66] worked on the core-shell structure of a metal-organic framework for the hybrid composite ZnO/$ZnCo_2O_4$/C synthesized through a hydrothermal route using $Co(acac)_2$, Zn $(NO_3)_2{\cdot}6H_2O$, 1,4-benzenedicarboxylic acid (H_2BDC) precursors, for hydrothermal treatment at 150 °C for 12 h. Finally heated at 400 °C for 1 h in the nitrogen atmosphere and again heated to 600 °C for 1 h in the air for the hybrid nanosphere formation. Yao *et al.* [67] prepared $CoMoO_4$ NPs/ rGO by hydrothermal route using prepared GO nanosheets, $Co(NO_3)_2{\cdot}6H_2O$ (4 mmol) and H_2MoO_4 (4 mmol), $NH_3{\cdot}H_2O$ were hydrothermally treated at 180 °C for 12 h. 3D architecture acts as an excellent scaffold to host 3-5 nm $CoMoO_4$. Lee *et al.* [68] synthesized $Zn_{1.67}Mn_{1.33}O_4$/graphene prepared using zinc acetate dihydrate (2 mmol), manganese acetate tetrahydrate (1.59 mmol), urea (20 mmol), ammonium bicarbonate (60 mmol), 100-mL ethylene glycol and isopropanol (IPA) in an autoclave for the solvothermal process. The resulting product was calcined at 500 °C for 2 h to achieve the final ternary compound. Sebastian *et al.* [69] have prepared Go-Fe/ZnO ternary compound via the hydrothermal method to prepare the honeycomb sort of ZnO particles and sonochemical route for the ternary composite. They added the macrocyclic Fe complex $[Fe(C_{10}H_{20}N_8)(H_2O)_2](BF_4)_2]$ solution dropwise to the prepared GO solution and allowed it to stir for 24 h. 3D honeycomb structures of ZnO prepared using zinc nitrate hexahydrate, HMT (hexamethylenetetramine) and trisodium citrate dihydrate. After tuning the morphological structure and intensely sonicating at 50 °C for 2 h in a high-intensity ultrasonic reactor, they achieved a homogeneous ternary composite.

Guofeng *et al.* [70] group developed rGO/Fe_2O_3/SnO_2 ternary nanocomposite via in-situ co-precipitation and hydrothermal method. Combination of $FeCl_3{\cdot}6H_2O$ and GO mixtures was sonicated for the precipitation formation and then transferred into an autoclave at 120 °C for 4 h to reduce GO. Then $SnCl_2{\cdot}H_2O$ was introduced under stirring and annealed at 400 °C for 1 h. Table 3 explains the list of CDTMOs composites prepared hydrothermally.

Table 3. *Hydrothermal synthesis of ternary composites*

No	Ternary composites	Operating conditions	Advantages	Ref.
1	SnO_2-Fe_2O_3-rGO	190 °C for 22 h	High porosity, surface area	[59]
2	rGO/Mn_3O_4/V_2O_5	180 °C for 24 h,	Large surface area due to Mn_3O_4 spheres, V_2O_5 rod nanostructures	[60]
3	CuO/RuO_2/MWCNTs	180 °C for 12 h	High crystallinity, narrow particles distribution	[61]
4	CeO_2–SnO_2/rGO	150 °C for 2h	Spherical particles,	[62]
5	SnO_2-Fe_2O_3/SWCNTs	180 °C for 48 h	High surface area, interconnected electron pathway	[63]
6	SnO_2/NiO/rGO	200 °C for 18 h	Unique hybrid nanostructures increased active sites	[64]
7	SnO_2-CuO/rGO	120-150 °C for 12 h	Synergistic effect among the NPs	[65]
8	ZnO/$ZnCo_2O_4$/C	150 °C for 12 h	Porous core-shell, synergistic effect abundant active sites	[66]
9	$CoMoO_4$/ rGO	180 °C for 12 h	3D architecture, as an excellent scaffold to host 3-5 nm $CoMoO_4$ particles	[67]
10	$Zn_{1.67}Mn_{1.33}O_4$/graphene	200 °C for 24 h	Porous structure of micro spheres particles tends to have a large surface area	[68]

Sol-gel method

Sol-gel method of synthesizing achieves nanosized particles with the optimized conditions to control the particles' growth. The sol-gel method is a cost-effective and eco-friendly method. The sol-gel method greatly impacts the engineering surface morphology. Establishing the inorganic network through colloidal suspension (sol) and gelation to obtain a gel network takes place [71,72]. Kose *et al.* [73] produced ZnO/ SnO_2/ MWCNT composite through sol-gel synthesized SnO_2/ZnO (shell) composite on MWCNT (core) in 3D bucky papers network by spin coating to fabricate the free-standing SnO_2/ZnO/ MWCNT ternary composite. Precursor of $Zn(CH_3COO)_2{\cdot}2H_2O$ was used to prepare ZnO sol by ethanol solvent and chelating with glycerin. SnO_2 sol synthesis using $SnCl_2{\cdot}2H_2O$ precursor through chloride removing route with chloride precipitation NH_3 solution. MWCNT buckypaper substrates were consecutively coated with the synthesized ZnO and SnO_2 sols by spin coating and finally calcined at 400 °C for 2 h in Ar atmosphere. Kose *et al.* [74] developed the architecture of ZnO-SnO_2-rGO via a sol-gel route with the precursors $SnCl_2{\cdot}2H_2O$ with Zn $(CH_3COO)_2{\cdot}2H_2O$, glycerin acts as a gelating agent to produce the homogeneous sol. Finally, the product was calcined at 500 °C for 2 hours, providing free-standing flexibility due to a synergistic effect.

Figure 3 explains the advantages and disadvantages of different wet-chemical routes

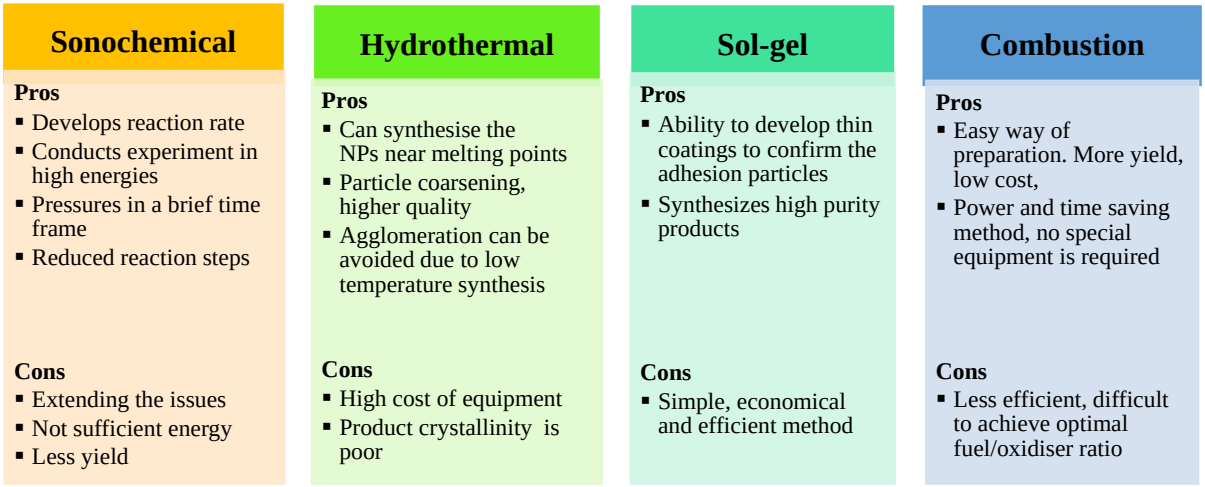

Figure 3. *Advantages and disadvantages of different wet-chemical routes*

Spectroscopic analysis of carbon derivatives based ternary metal oxide (CDTMOs) composites

This section discusses the characterization of CDTMOs composites. The primary analysis for the confirmation of elemental presence in the prepared material has been achieved by advanced analyzing tools such as X-ray diffractometer (XRD), Raman spectroscopy and Fourier transform infrared spectroscopy (FTIR). XRD is the main spectroscopic technique for the preliminary confirmation of the material and identifies the phase structure and crystallinity of CDTMOs. Research papers revealed that the XRD failure to locate rGO peaks might be due to low intensity or the complete reduction of GO, so further Raman studies can confirm the presence of carbonaceous materials [75]. Therefore, hereby we discussed the XRD and Raman spectroscopic techniques for the chemical and structural characteristics of CDTMOs.

X-ray diffractometer (XRD)

In this spectroscopic analysis, we discuss the XRD patterns of CDTMOs, mainly focused on carbonaceous materials. XRD 2θ values of carbonaceous materials and phase structures of CDTMOs

composites are tabulated in Table 4. In MgO/NiO/graphene ternary composite, the carbon diffraction peak located at 26.4° indexed as (002) plane of the hexagonal phase. The crystalline constituents are not clear from the XRD analysis. Therefore, the SAED pattern of TEM confirms the presence of multi-layered graphene [54]. In Co_3O_4/CeO_2/CNTs composite, the CNT peak is at 26° for the (002) plane [76]. In the SnO_2-Fe_2O_3-rGO ternary composite, the 2θ diffracted peaks centered at 11 and 43° for (001) and (002) GO planes. Fe_2O_3 exhibits the presence of a two-phase composite. Compared to individual compounds, ternary composite peaks were shifted slightly at lower positions, the intensity of the diffracted peak decreased and broadened the peak width was based on the GO addition [59]. The intensity of the rGO/TiO_2/ZnO ternary composite's diffracted peaks was decreased and the width of the peak broadened when the amount of GO increased in the composite, which signifies the interaction of rGO in the TiO_2/ZnO composite. For graphite, a sharp peak occurred around 11.63° representing the (001) plane and a peak at 26° representing the (002) plane. In rGO formation, the characteristic peaks of GO disappeared and a new peak formed at 23.61°, indicating a reduction of GO to rGO. The corresponding lattice spacing value of 0.760 nm reduces to 0.336 nm, which confirms the oxidation [77].

Table 4. *Structure and 2 theta information of ternary composites*

No.	Ternary composites	Carbon derivatives, 2θ / ° (hkl)	Structures	Ref.
1	rGO-TiO_2-ZnO	G -26.5 (002) GO- 11.63 (001) rGO- 23.61	ZnO-hexagonal phase, wurtzitestructure, graphite-hexagonal	[77]
2	MgO-NiO-Graphene	C- 26.4 (002)	MgO-Cubic, NiO-cubic, graphene-hexagonal	[54]
3	Co_3O_4/CeO_2/CNTs	CNT -26 (002)	Co_3O_4 -Cubic	[76]
4	SnO_2–Fe_2O_3-rGO	GO -11 (002), 43 (100)	SnO_2-tetragonal rutile	[59]
5	rGO/Mn_3O_4/V_2O_5	GO- 10 (001)	Mn_3O_4-orthorhombic, V_2O_5-orthorhombic	[60]
6	CeO_2–SnO_2/rGO	G -26.4, GO- 11.4 (001)	CeO_2-cubic, SnO_2-tetragonal	[62]
7	ZnO-SnO_2-rGO	rGO- 26 (002)	ZnO-hexagonal, SnO_2-cassiterite	[74]
8	$CoMoO_4$/ rGO	rGO -26 (002)	$CoMoO_4$-monoclinic	[67]
9	CNT@Fe@SiO_2	CNT- 26.4 (002)	Fe-cubic	[78]
10	Ag/TiO2/CNT	No peak for CNT	TiO_2-anatase phase	[79]
11	SiO/Ni/Graphite	Graphite- 26.2 (002)	Ni-face centered cubic, graphite-hexagonal	[80]
12	Cu_2O-CuO-rGO	rGO- 25 (002)	-	[82]
13	CuO-ZnO/rGO	GO- 10.5 (001), rGO -23.72 (002)	CuO-monoclinic ZnO-wurtzite	[83]
14	NiO-ZnO/RGO	rGO -26 (002)		[29]
15	WO_3-ZnO@rGO	-	WO_3-monoclinic, ZnO-hexagonal wurtzite	[84]
16	ZnO-rGO/RuO_2	-	ZnO-hexagonal wurtzite, RuO_2-rutile	[85]
17	CNT/SiO_2/MoO_3	CNT -25.9 (002), 43.3 (110)	-	[86]

The conversion of graphite to GO is indicated by the characteristic peak located at 10° with the 0.87 nm d-spacing value in the rGO/Mn_3O_4/V_2O_5 ternary composite. The characteristic peaks were shifted due to composite formation [60]. In the CeO_2–SnO_2/rGO ternary composite, the diffracted peak shifted to a lower angle side at 11.4° compared to the graphite peak located at 26.4°. This confirms the oxidation of GO and reduction of GO by the 22.4° for the (002) plane [62]. In the ZnO-SnO_2-rGO ternary composite, broadened rGO peak located at 26° confirms the reduction of GO

represents the (002) plane [74]. In $CoMoO_4$/ rGO ternary composite, the formed broad peak attributed to the (002) plane of the rGO, but in the XRD of the ternary composite, rGO disappeared, indicating the rGO flakes were well separated by the $CoMoO_4$ NPs. The intensity of the ternary composite peaks was stronger by increasing the $CoMoO_4$ addition. The characteristic peak of the rGO did not appear in the ternary composite. This could be due to lower intensity and less quantity of GO. Raman is the best characterization technique to confirm rGO [67]. In the CNT@-Fe@-SiO_2 ternary composite, the CNT characteristic peak at 26.4° for the (002) plane was quite diminished in the XRD of the composite [78]. In Ag/TiO_2/CNT ternary composite, no diffraction peaks were noticeable in the composite XRD plot due to the shielding of the MWCNT peak at 26.1° by the anatase peak of TiO_2 located at 25.3°. Because of the low amount of MWCNT presented in the composite, MWCNT exhibited low intensity compared to TiO_2 [79]. In SiO/Ni/graphite ternary composite, a sharp peak located at 26.2° was assigned to the hexagonal (002) plane of graphite. The initial amorphous nature of the SiO/Ni gained crystallinity upon the addition of graphite, which displayed sharp diffraction peaks [80]. XRD pattern of CNTs@TiO_2/CoO ternary composite is shown in Figure 4. Rutile Braggs positions were labeled in the XRD pattern, which corresponds to the higher temperature required for the CNTS formation by spray pyrolysis [81].

In the Cu_2O-CuO-rGO ternary composite, (002) plane represents the rGO nanosheets. Diffracted peaks of two copper phases (CuO and Cu_2O) were present in the XRD pattern [82]. CuO-ZnO/rGO ternary composite films showed a strong characteristic peak at 10.5° attributed to the (001) plane. This peak disappeared for rGO and formed one broad peak at 23.72° for the (002) plane. Ternary composite peaks have represented low intensities due to the low contents of the precursors [83]. In NiO-ZnO/RGO composite, diffracted peaks explained the NiO, and ZnO characteristic peaks and a broad peak centered at 26° explains the graphene stock disorder [29].

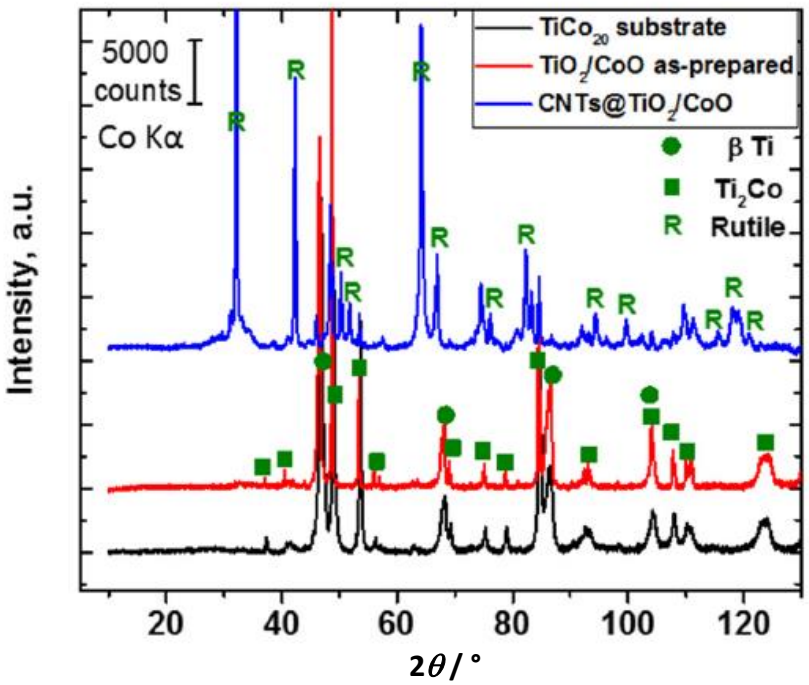

Figure 4. *XRD pattern of CNTs@TiO_2/CoO ternary composite (MDPI Open access journal [81])*

In WO_3-ZnO@rGO, peaks corresponding to WO_3, and ZnO appeared as per the standard JCPDS card numbers, but no peak for rGO represents unstacked rGO sheets. The intensity of the characteristic peaks depends on the precursor content ratio. Especially, no characteristic diffraction peaks for the

distinct GO are seen, which may be caused by the low quantity and low diffraction intensity of GO or by the full elimination of GO by the synthesis process during the formation of ZnO [84]. In the case of ZnO-rGO/RuO_2, no GO peaks due to the low intensity or complete reduction of GO [85]. In CNT/SiO_2/MoO_3 composite, 25.9 and 43.3° diffraction peaks correspond to the (002) and (110) planes of carbon materials. MoO_3 sharp peaks represented the highly crystalline and broadened SiO_2 peaks for the amorphous nature of the ternary composite [86]. We can understand that bulge/broad peaks explain the amorphous nature. The addition of carbonaceous materials into the metal oxide matrix could decrease the size of the particles and make it possible to achieve uniform particles. The interplanar spacing value will be increased upon the incorporation of carbonaceous materials. The characteristic peak of graphite increased with increasing graphite content in the composites. The more active phases of the materials more likely it is to accommodate volume changes during redox reactions of the LIBs. But active phases can also contribute to the feasible topotactic activity.

Raman spectroscopy

Raman spectroscopy is a non-invasive, near-surface non-destructive technique. Its analysis provides information about a material's composition or properties. To identify and quantify the functional moieties and covalency of the attached carbon frame has been carried out through the Raman analysis [87]. Below, we discussed the Raman analysis of the carbonaceous materials in the ternary composites.

In Co_3O_4/CeO_2/CNT ternary composite, two dominant Raman peaks at 1332 and 1588 cm^{-1} represent the D and G bands. D band signifies the defective structure or disordered carbon. The G band signifies the tangential modes of graphitic layers. The degree of graphitization is measured by the ratio of D-band intensity to G-band intensity (I_D/I_G) and is used to estimate the defect density. The ratio (I_D/I_G) of the composite material was 1.49, which explains CNTs were highly disordered, and the introduction of metal oxides doesn't change the CNT's degree of the disorder [76]. Raman modes of the disordered D band located at 1335 cm^{-1} indicated the defects in sp^2 hybridized carbon and G band at 1587 cm^{-1} indicated the vibration mode of sp^2 bonded carbon. The D and G band values were in accordance with the formation CNTs [81].

In the rGO/TiO_2/ZnO ternary composite, GO is represented by 1356 and 1586 cm^{-1} Raman characteristic modes represented as D and G bands. The ratio of I_D and I_G is 0.99. The ratio value increased to 1.21 in the case of rGO explains the decrease in the average size of sp^2 domains and increases the defects in rGO ternary composite. The relation between the integrated intensities of disordered-induced Raman bands (I_D/I_G) with the different crystallite sizes (L_a) is explained by the equation (1):

$$L_a = 2.4\times10^{-10}\,\lambda_1^4\,(I_D / I_G)^{-1} \quad (1)$$

where λ_1 represents the excitation wavelength (514.5 nm), L_a represents the sp^2 domain size. As per the calculated domain sizes of GO (16.98 nm) and rGO/TiO_2/ZnO (13.89 nm), size was reduced in the ternary composite compared to GO. The primary cause of this size reduction is the reduction of surface epoxy groups, which has resulted in the conversion of GO to rGO. Therefore, the increase in the I_D/I_G ratio's intensity is due to the reduction in the sp^2 domains' average size [77]. In the rGO-ZnO-TiO_2 ternary nanocomposite, the D and G bands correspond to the k-point photons of A_{1g} symmetry and the E_{2g} phonon resulting from sp^2 C atoms, corresponding to 1339 and 1594 cm^{-1} Raman modes. GO shows the prominent Raman modes at 1356 and 1586 cm^{-1}, termed as D and G bands, also ascribed as modes of k point modes of the A_{1g} symmetry involving phonons near boundary and scattering of first order E_{2g} phonon of carbon atoms [88]. In the MgO-NiO/ graphenaceous ternary compound, the presence of D mode demonstrated the disorder. These sp^2-bonded carbon nanostructured materials

exhibited the G band, which provides information about in-plane vibrations. In MgO-NiO decorated graphenaceous materials D, G, G^*, 2D, D+G and 2D' bands representative of typical multi-walled carbon nanotubes [54]. In ZnO-SnO_2-rGO Raman spectrums, the G band (around 1590 cm^{-1}) arises from sp^2 C atoms and the D band (around 1350 cm^{-1}) originates mainly from sp^3. Carbon atoms are based on defects found at the end of graphite and graphene layers. The I_D/I_G ratios for MO/rGO composites were greater than that of rGO, which suggests that structural change was increased [74]. In Ag/TiO_2/CNT ternary composite, the intensity of the characteristic modes was decreased compared to TiO_2 modes, which may be due to the addition of Ag NPs. Two prominent Raman modes occurred at 1360 and 1579 cm^{-1}, for the D and G bands of MWCNT [79]. In SiO/Ni/Graphite ternary composite, two characteristic bands at 1356 and 1583 cm^{-1} are in good agreement with the typical Raman modes for the D and G bands of graphite, respectively [80]. In the Cu_2O-CuO-rGO ternary composite, D-band (1346.9 cm^{-1}) and G bands (1583.5 cm^{-1}) represented the rGO nanosheets. The intensity ratio of the ternary composite was higher than the pure rGO, which signifies more defects in the composite [82]. In Co_3O_4-ZnO/rGO composite, the two main intrinsic Raman peaks, in that D band centered at 1358 cm^{-1} aroused due to the breathing mode of k-point photons, and another one due to A_{1g} symmetry and due to the first-order scattering of E_{2g} phonon of sp^2 carbon atom formed G band centered at 1584 cm^{-1} [89]. In CNT/SiO_2/MoO_3 ternary composite, there were two unique peaks: the peak at 1597 cm^{-1} was associated with the C=C backbone stretching (G band), and the peak at 1336 cm^{-1} was associated with the D band. The ratio of I_D/I_G is slightly greater than 1, but if it is less than 1, as in the case of CNT, more defects and lower crystallinity in the ternary composite than in CNT can be found [86]. Raman spectroscopic information revealed that the carbon-related prominent Raman modes are designated as D-band and G-band, representing the structural defects disorder and in-plane vibrations of sp^2-bonded carbon atoms. The presence of these bands confirms the interfacial interaction between the MOs and carbon materials. Table 5 explains the peak positions and I_D/I_G ratio information of ternary composites.

Table 5. *Peak positions and I_D/I_G ratio information of ternary composites*

No.	Ternary composites	Raman peak positions	I_D/I_G ratio	Ref.
1	rGO-TiO_2-ZnO	D-1356, G-1586	GO 0.99, Ternary 1.21	[77]
2	Co_3O_4/CeO_2/CNT	D 1332, G 1588	Ternary 1.48	[76]
3	ZnO-SnO_2-rGO	-	GO 1.1263, rGO 1.286, Ternary 1.411	[74]
4	Ag/TiO_2/CNT	D-1350, G-1579	-	[79]
5	SiO/Ni/Graphite	1356, G-1583	-	[80]
6	Cu2O-CuO-rGO	D-1346.9, G-1583.5	rGO 1.16, Ternary 1.38	[82]
7	CNT/SiO_2/MoO3	G-1597, D-1336	CNT <1, Ternary >1	[86]
8	Co_3O_4-ZnO/rGO	D-1358, G-1584	GO 0.83, Ternary 0.92	[89]
9	CNTs@TiO_2/CoO	D-1335, G-1587	-	[81]

Microscopic analysis of carbon derivatives based ternary metal oxide (CDTMOs) composites

Versatile topographical information of the CDTMOs composites was examined with scanning electron microscopy (SEM), field-emission scanning electron microscopy (FESEM) and transmission electron microscopy (TEM). Morphology information includes surface features, shape, size and structure of the compounds. SEM provides digital image resolution as low as 15 nm and instructive data about the characterization of microstructure, including morphology, roughness, and boundaries [90]. FESEM provides morphological images of higher magnifications [91]. TEM can produce a much higher resolution of quality images than SEM and SAED (selected area electron diffraction)

for crystallinity confirmation. Morphological variations of structures can be performed during the synthesis through the usage of surfactants, reducing agents, protecting agents (PVA in DMF) and optimizing the experimental parameters such as experiment duration, temperature and so on [92].

The nanowires are typically tens to hundreds of microns long, randomly orientated, and have either curved or straight morphologies. The aspect ratio of nanowires is high, and their diameter is around 10 nm. Long aspect ratio particles are considered nanowires [93]. The ternary nanocomposite of rGO/MoO_3@C morphology explored by carbon-coated uniformly straight α-MoO_3 nanowires of 6-8 µm length and diameter of 100-150 nm along with the intertwined rGO nanosheets as per FESEM. TEM revealed that the graphene sheets were homogeneously wrapped on MoO_3@C nanowires [94]. There are many more nanowires sort of structures available as battery materials for LIBs, including Co_3O_4 nanowires [95], Co_3O_4/NiO/C [164] and so on.

Nanorods are 1-D nanostructures and synthesis is more flexible. Nanorods typically range in length from 10 to 120 nm. Metal oxide nanorods are effectively created by converting nanoparticles at a comparatively low temperature of 80 °C [96]. Examples of nanorods include the Co-Ni-based ternary molybdate nanorods [97], Co_3O_4 nanorods [98], α-MoO_3@ MnO_2 core-shell nanorods [99].

Figure 5 demonstrates the highly-magnified image of the CNTs@TiO_2/CoO nanotubes. The figure explains the effective connection of CNTs with the TiO_2/CoO nanotubes and displays a web-like structure [100].

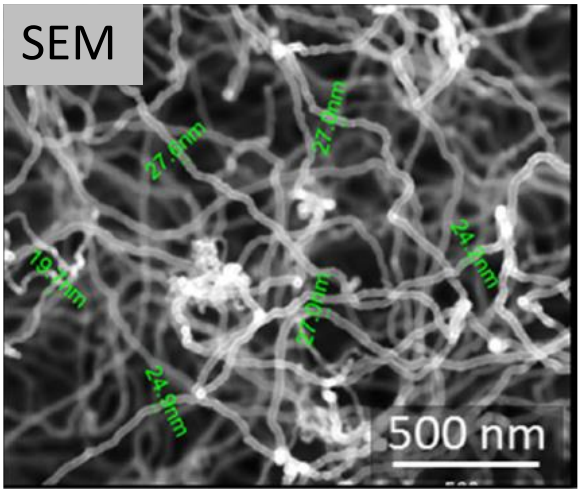

Figure 5. *SEM image of CNT@TiO_2/CoO composite (Open access MDPI journal [100])*

Two-dimensional (2D) inorganic nanosheets have attained great attention of study because of their unusual characteristics, such as a high degree of anisotropic morphology and increased surface area with numerous surface-active sites, and distinctive electronic structures [101].

Cu_2O/CuO/rGO ternary composite was explored in the 3D hierarchical structure, in that CuO displayed a sheet-like structure of average 500 nm width. In this, Cu_2O/CuO was wrapped by rGO layers [102]. In rGO/SnO_2/Au nanocomposite, the introduction of rGO relieved the aggregation of SnO_2 nanosheets. Therefore, SnO_2 formed homogeneously on rGO with the Au NPs as per the FESEM [103]. In NiO- SnO_2/rGO, as per SEM and TEM results, NiO-SnO_2 particles are distributed on graphene nanosheets with different magnifications. NiO-SnO_2 of different particle sizes exhibited no fixed dimensions and rGO exhibited plate-like crumpled features [104]. SnO_2/MoO_3/C ternary composite was composed of SnO_2-MoO_3 and graphite nanosheets. TEM revealed that SnO_2 and MoO_3 NPs are between 5-10 nm in size and equally wrapped in plate sort of graphite [105]

MoO_3 exhibits a nanobelt structure and are completely dispersed in the rGO layer in the ternary composite of MoO_3/Fe_2O_3/rGO, according to the FESEM. TEM revealed that the width of nanobelts ranges between 50 and 100 nm, and the length ranges from several hundreds of nanometers to several tens of micrometers [106]. CuO-ZnO/rGO ternary composite displayed unique architecture consisting of CuO 1D nanochains and ZnO nanoseeds of average length ~674 nm, and average width 287 nm. Highly magnified rectangular seeds are of average size of 20.4 nm. ZnO nanoseeds dispersed on the rGO sheets and interlinked with CuO nanochains [83].

Nanoflakes exhibit porous structures created by a group of a large number of NPs. NiO-ZnO/rGO composite composed of many thin curly flakes and few discrete particles covered with graphene sheets indicated uniform distribution. Loosely packed NiO-ZnO formed on the high surface rGO sheets [29]. Examples of nanoflakes sort of structures are SnO_2@ MnO_2 nanoflakes [107].

Nanospheres possess uniform structures, consisting of spherical particles with diameters between 10 and 200 nm, and exhibit various new, improved size-dependent features, which exhibit a conventional core-shell structure compared to bulk spheres nanospheres/microspheres. In V_2O_5/rGO/CNT ternary composite, TEM revealed that the V_2O_5 microspheres of 1 µm were embedded in rGO/CNT matrix. Composite described the penetration of CNT into V_2O_5 assembly, representing the homogeneous distributions of V, O and C [108]. Quasi-nanospheres of SnO_2/TiO_2/C, spherical hollow structure of SnO_2-TiO_2-C, micro hollow spheres of $ZnO/ZnFe_2O_4$ /N-doped C, hollow hybrid nanospheres of SnO_2@C@MnO_2, and SnO_2/TiO_2 spheres are good examples [109,110].

Ternary Co_3O_4-ZnO/rGO composed of cubic-shaped Co_3O_4 particles and hexagonal disks-shaped ZnO particles were anchored on the rGO sheets as per FESEM and TEM [89]. CNT/SiO_2/MoO_3 composite contains cactus-shaped structure composed of a large number of CNTs in the form of cactus leaves, which are 0.5 to 2 µm in length and 3 to 30 nm in diameter. In this, SiO_2 and MoO_3 were present on the surface of cactus according to SEM and TEM [86]. Co_3O_4 performs the nanocage sort of structure [112], flower type of structure can be noticeable in Co_3O_4 [111]. WO_3-ZnO@rGO ternary composite displayed stacked nanopetals sort of structure, consisting of different sized WO_3 and ZnO nanorods. The increased magnified image revealed that the WO_3 consists of agglomerated nanocuboid of average dimensions 165/1533/73 nm^3. FESEM explains the two varied morphologies of spherical-shaped nanorods with infrequent nanowires for ZnO. The average diameter of nanowires and nanorods were estimated as 54 and 118 nm, respectively [84].

Figure 6 represents the SEM images (a and b) of ternary Fe_2O_3/TiO_2/C fibers with different magnifications. After the application of carbon, the composite showed a smooth surface fiber morphology [100].

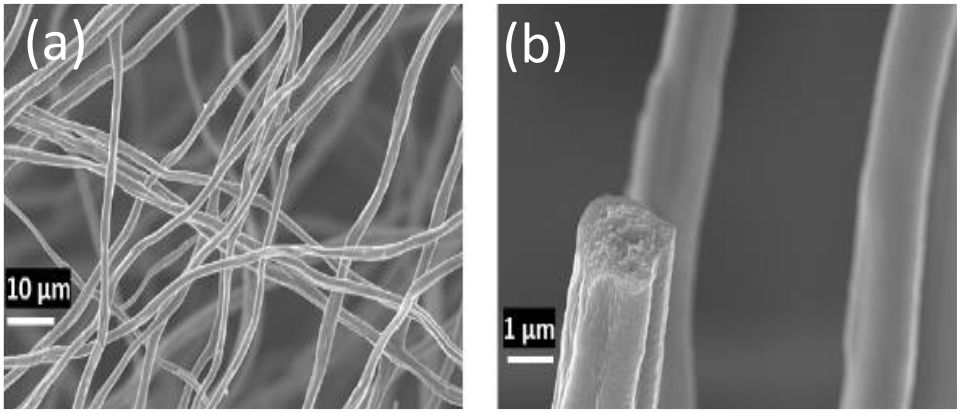

Figure 6. *SEM images of α-$Fe_2O_3TiO_2$/C fibers with different magnifications*

Unique structures promote feasible electron transportation by reversible redox reactions during the lithium-ion intercalation-deintercalation process. Volume expansion can be reduceable effectively by the feasible redox reactions. Mesoporous and microporosity structures contributed to the increase in the surface area. Carbonaceous materials provide fast electron transfer activity and excellent conductivity. The nanosheet structure of the composite helps to avail the large spacing to transfer the Li ions efficiently.

Electrochemical analysis of CDTMOs

The electrochemical performance of the LIBs will be measured by the discharge-charge capacity, rate capability for different C-rates or current density and cyclic stability. Discharge-charge curves of a battery cell are measured with respect to the specific voltage and current. The C-rate refers to how fast the battery is being charged or discharged. Lifetime and performance of a battery are drastically affected by the high C-rates. Battery cycling tests are carried out for the analysis of long-term stability [113]. Decomposition of the electrolyte or degradation of the electrode materials within the coin cell might reduce battery performance. Incomplete or slow rection kinetics of the redox reactions during the discharge-charge cycles leads to volume expansion of the cell, which might be detrimental to cyclic stability [114]. Graphite anode will react with the electrolyte and aggregate the lithium, reducing the battery performance and causing safety-related issues such as thermal runaway, exacerbating low-temperature operations. Electron and lithium-ion transportation is hampered by the weak conductivity of the electrode materials [115].

In recent years, extensive research has been conducted to develop novel composite materials with unique nanostructures. Novel architectures act as potential electrodes for improved electrochemical performance. Different combinations of the electrode materials could elucidate the battery materials' degradation during the charging-discharging process. Various synthesis methods are developed to improve the electrochemical performance. Nano-scaled particles of porous structures reduce the Li^+ diffusion length enabling the feasible Li-ion insertion-extraction mechanism [116].

First cycle Coulombic efficiency or FCE usually refers to the ratio of the discharge capacity after the full charge and the charging capacity. FCE will be significantly different from its subsequent cycles. The intercalated lithium ions do not leave the electrode completely during subsequent cycles. When the cell is discharged for the first time, impeded lithiation reaction takes place called SEI film before the Li ions insertion. Those lithium ions cannot be returned during subsequent charging cycles. The Coulombic efficiency of the battery is affected by the electrolyte decomposition, material aging, ambient temperature, and different charge-discharge current rates [117].

In this section, we discussed the electrochemical performance of selective promising metal oxides such as SnO_2, ZnO, MoO_3, SiO_x and others. Among the mentioned, one MO is fixed, and the second compound is any other metal oxide, along with any carbon derivative, to form ternary composites. Figure 7 shows the Schematic representation of carbon derivatives based ternary metal oxides.

Electrochemical performance of SnO_2 and carbon derivatives based ternary composites

Tin oxide (SnO_2) is propitious electrode material that serves as an anode in the LIBs because of its high theoretical capacity of 790 mAh g^{-1}, safety, and stability. SnO_2 alone suffers from structural integrity, intrinsic conductivity, rate capability and volume expansion [39]. The general electrochemical rection mechanism of SnO_2 electrode for LIBs is presented in Equations (2) and (3) [40].

$$SnO_2 + 4Li^+ + 4e^- \rightarrow Sn + 2Li_2O \quad (2)$$

$$Sn + xLi^+ + xe^- \leftrightarrow Li_xSn \quad (3)$$

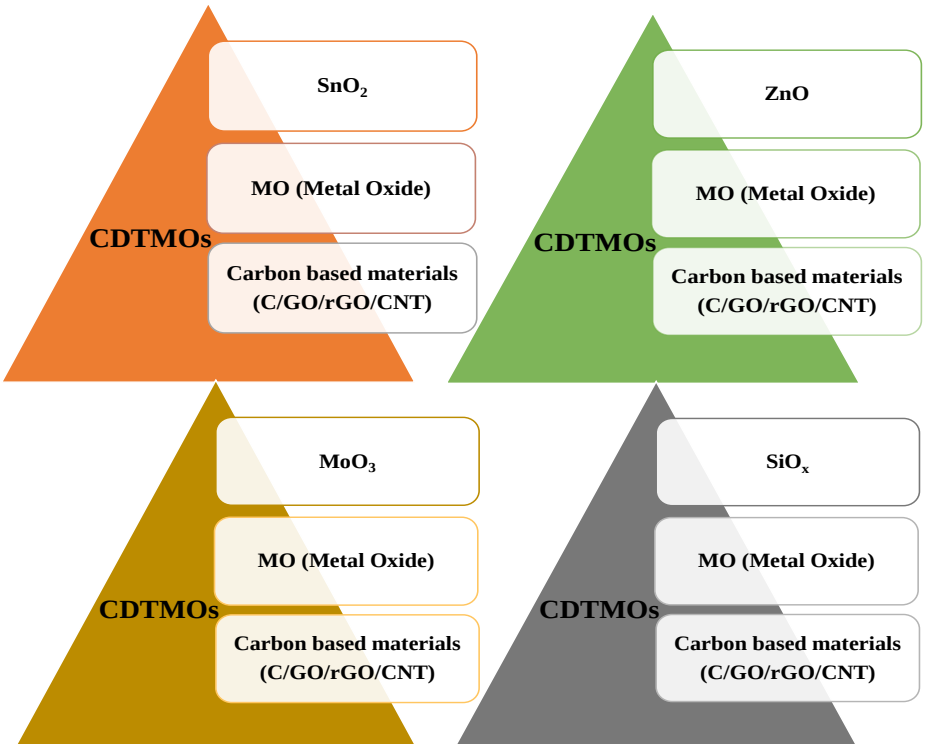

Figure 7. *Schematic representation of carbon derivatives based ternary metal oxides*

Here, in this case, reaction (1) represents the conversion reaction. It is irreversible and responsible for the initial capacity fading. Equation (2) represents the alloying-dealloying reaction, which is reversible and contributes dominant capacity for the LIBs [40]. Many SnO_2-based ternary composites are explored in the literature. Ternary composites of two MOs electrode materials along with the carbon derivatives undergo a synergistic effect. The synergistic effect plays an important role in the ternary composite by adding up each compound's advantages. Porous carbon materials act as a buffer matrix to overcome the volume expansion. However, ternary composites are less exposed compared to binary composites.

Xia *et al.* [70] fabricated SnO_2/Fe_2O_3/rGO anode through homogeneous precipitation method. As per TEM analysis, Fe_2O_3 NPs surrounded SnO_2 NPs. SnO_2 particles prevented the agglomeration of Fe_2O_3 NPs. Feasible ions transportation and stress relieving took place during charge-discharge process. This novel composite initially exhibited an 1179 mAh g^{-1} discharge capacity at a current density of 400 mA g^{-1} and maintained a stable 700 mAh g^{-1} capacity. In another work, the same composition, SnO_2-Fe_2O_3/rGO was designed by Zhu *et al.* [118] through a facile wet-chemical solvothermal approach. They maintained the weight ratios (SnO_2: Fe_2O_3: rGO is 11:1:13) in the ternary composite. Composite exhibited the controlled phase ratio, which depicted the higher specific capacity of 958 mAh g^{-1} at 0.5 C (395 mA g^{-1}) current density even after 100 cycles and high rate capability of 530 mAh g^{-1} at 5 C (3950 mA g^{-1}). Significant discharge capacity at higher current density was attributed to the addition of a small quantity of amorphous Fe_2O_3. The combination of Fe_3O_4 with SnO_2 and rGO ternary composite prepared by Wang *et al.* [119] via the hydrothermal method, Fe_3O_4 and SnO_2 NPs uniformly loaded on rGO nanosheets without aggregation prepared. The ternary composite of SnO_2/Fe_3O_4/rGO displayed higher capacity than its binary counterparts due to the benefits of the synergistic effect between SnO_2 and Fe_3O_4 by achieving superior cyclic stability. Smaller crystallite size facilitated Li-ion transportation and reduced the diffusion path. This composite exhibited a higher reversible capacity of 947 mAh g^{-1} at 200 mA g^{-1} current density in the initial cycle, maintaining a capacity of 831 mAh g^{-1} after 200 cycles. This composite experienced faster capacity fading by increasing the current density.

Along with SWCNT, the same SnO_2-Fe_2O_3 was developed by Wu *et al.* [120] through the hydrothermal method. In this case, SnO_2 and Fe_2O_3 NPs homogeneously settled on the surface of SWCNT. SnO_2-Fe_2O_3/SWCNT ternary composite exhibited the specific capacity of 692 mAh g^{-1} after 50 cycles at 200 mA g^{-1} current density and at a higher current density of 2000 mA g^{-1} electrode was capable of delivering 656 mAh g^{-1}. The good electronic conductivity and flexible mechanical strength of the SWCNT are the main reasons for the improved rate capability and reduced volume expansion. Joshi *et al.* [121] have engineered the flexible and freestanding Fe_2O_3-SnO_x-carbon nanofiber composite by electrospinning method. Fe_2O_3-SnO_x-C nanofiber of weight ratio (Fe:Sn/3:1) exhibited 756 mAh g^{-1} after 55 cycles and 540 mAh g^{-1} specific capacity at a higher current density of 1000 mA g^{-1} due to accommodating the volume changes of Fe and Sn by carbon nanofiber.

Hilal *et al.* [122] prepared SnO_2/ZnO/MWCNT composite by sol-gel and spin coating method. This anode maintained a high capacity of 487 mAh g^{-1} after 100 cycles. The authors explained the advantages of individual compounds and the impact of high surface area, mesoporous nature, and electronic properties**.** Kose *et al.* [74] have developed the architecture of SnO_2-ZnO-rGO via a sol-gel wet chemical route. They also confirmed that the ternary composite delivered higher performance than the binary electrode. SnO_2-ZnO material was designed between rGO layers. Superior properties of each compound contributed to enhancing electrochemical activity attributed to the synergistic effect, which delivered 731 mAh g^{-1} specific capacity after 100 cycles at 0.2 C-rate and displayed good rate performance.

Ternary SnO_2-MoO_3-C nanosheet structure was prepared using hydrothermal and dry ball milling by Feng *et al.* [105]. SnO_2/MoO_3 NPs were encapsulated in plate graphite to exhibit the nanosheet structure. MoO_3 additive protected Sn from aggregation and nano-sized composite provided more active sites. SnO_2-MoO_3-C electrode exhibited the outstanding discharge capacity of 1338.3 mAh g^{-1} at 200 mA g^{-1} after 300 cycles and stable rate performance carried out at a current density of 5000 mA g^{-1} delivered 715.08 mAh g^{-1}. One more important notable thing is they used lamina sort of graphite, which alleviated the volume expansion and reduced the Li-ion transportation distance, therefore displaying remarkable electrochemical performance.

Huang *et al.* [64] prepared a graphene-supported porous SnO_2/NiO ternary composite via a hydrothermal route. A special structure increased the electronic conductivity and buffered the volume expansion. This composite exhibited the 1280 mAh g^{-1} initial discharge capacity at 300 mA g^{-1} current density and maintained 410.74 mAh g^{-1} after 50 cycles, also achieving 99.4 % of coulombic efficiency.

Hydrothermally synthesized SnO_2-TiO_2@graphene ternary composite was prepared by Jiao *et al.* [124]. Unique structures of SnO_2 and TiO_2 were grown on graphene. It exhibited 1276 mAh g^{-1} discharge capacity even after 200 cycles at 200 mA g^{-1} current density and produced 611 mAh g^{-1} capacity at high-rate of 2000 mA g^{-1}. The comparative study was performed with SnO_2, GO, and SnO_2-TiO_2@graphe [125-128]**.**

Quasi-nanospheres of SnO_2/TiO_2/C were developed by D. Bao *et al.* [129] through the hydrothermal method. In this case, SnO_2 NPs sandwiched between TiO_2 quasi nanospheres and carbon coating presented a sphere structure in between the gaps. More spaces can effectively accommodate Li^+ ions and reduce the aggregation of the particles. Composite exhibited 895.3 mAh g^{-1} specific capacity after 70 cycles at 100 mA g^{-1} current density and maintained a 347.3 mAh g^{-1} reversible capacity at 3000 mA g^{-1} higher current density due to the improved reaction kinetics.

Zhao *et al.* [65] developed SnO_2-CuO/graphene synthesized via a hydrothermal route composed of CuO nanorods uniformly loaded on graphene nanosheets. It maintained 584 mAh g^{-1} at 0.1 C after 30 cycles.

Agubra *et al.* [130] developed SnO_2/NiO/C composite nanofiber by force spinning followed by a subsequent thermal treatment method called carbonization. This electrode directly acted as a working electrode without a current collector, binder and conducting additives. In this study, they compared SnO_2/NiO/C and Sn/C composites and confirmed that the SnO_2/NiO/C composite delivered higher performance than Sn/C. SnO_2/NiO/C exhibited 677 mAh g^{-1} specific capacity even after 100 cycles at 100 mA g^{-1} current density.

Yukun *et al.* [131] synthesized SnO_2-Co_3O_4-C composite through the hydrothermal method followed by two-step ball milling by uniformly anchored SnO_2 and Co_3O_4 NPs on the graphite nanosheets. This composite exhibited a stable capacity of 842 mAh g^{-1} even after 300 cycles at 0.2 A g^{-1} and retained a discharge capacity of 596.1 mAh g^{-1} after 980 cycles at 1 A g^{-1}.

Wang *et al.* [132] synthesized the ternary composite of SnO_2@C@MnO_2 through the reflux method. The structure is composed of the coating of MnO_2 nanosheet-based shell on SnO_2@C hollow nanospheres. The ternary composite SnO_2@C@MnO_2 exhibited a discharge capacity of 644.5 mAh g^{-1} after 200 cycles at 100 mA g^{-1} current density and maintained 434.2 mAh g^{-1} specific capacity at a current density of 1000 mA g^{-1}. The better electrochemical performance was attributed to the rational design of hierarchical nanostructures. Li *et al.* [133] developed SnO_2@MnO_2@graphite through facile ball-milling followed by a hydrothermal method. The graphite nanosheets contributed to good conductivity and minimized the volume expansion. The SnO_2@MnO_2@graphite exhibited a specific capacity of 1048.5 mAh g^{-1}, a superior rate capability of 522.2 mAh g^{-1} at a current density of 5.0 A g^{-1} and maintained a stable long-life cyclic performance of 814.8 mAh g^{-1} at 1.0 A g^{-1} even after 1000 cycles. Along with the SnO_2 electrode material, MoO_3 and TiO_2 are good substituting metal oxides for achieving the improved electrochemical performance of LIBS. Lamina sort of graphite incorporation enhanced the rate capability by reducing the volume expansion. Unique structures of SnO_2-Fe_2O_3 imposed on rGO sheets displayed high discharge capacity. SnO_2-MnO_2-graphite, SnO_2-MoO_3-C and SnO_2--TiO_2@rGO ternary composites delivered superior cyclic stability among the cited literature in Table 6.

Table 6. *Electrochemical performance of the CDTMOs associated with SnO_2*

No.	Ternary composites	Synthesis methods	Initial discharge capacity, mAh g^{-1}; Current density, mA g^{-1} or C-rate	Specific capacity, mAh g^{-1} / cycles; Current density, mA g^{-1} or C-rate	Rate capability, mAh g^{-1}, Current density, mA g^{-1} or C-rate	Ref.
1	SnO_2-Fe_2O_3/rGO	Precipitation	1179; 400	700/100; 400	139, 5 C	[70]
2	SnO_2-Fe_2O_3/rGO	Solvothermal	1509; 395/ 0.5 C	958/100; 0.5 C	530; 3950	[118]
3	SnO_2/Fe_3O_4/rGO	Hydrothermal	947; 200	831/200; 200	50; 5000	[119]
4	$SnO_2Fe_2O_3$/SWCNTs	Hydrothermal	1541; 200	692/50; 200	656; 2000	[120]
5	SnO_2-Fe_2O_x-carbon	Electrospinning	1053; 100	756/55,100	540; 1000	[121]
6	SnO_2/ZnO/MWCNT	Sol-gel, spin coating	1287; 0.2 C	487/100; 0.2 C	-	[122]
7	SnO_2-ZnO-rGO	Sol-gel	1702; 0.2 C	731/100, 0.2 C	150; 1C	[74]
8	SnO_2-MoO_3-C	Hydrothermal, ball milling	2057.5; 200	1338.3/300; 200	715.08, 5000	[105]
9	SnO_2/NiO @rGO	Hydrothermal	1280; 300	410.74/50, 300	-	[64]
10	SnO_2-TiO_2@rGO	Hydrothermal	2170; 200	1276/200; 200	611; 2000	[128]
11	SnO_2/TiO_2/C	Hydrothermal	1508.1; 200	895.3/70; 100	347.3, 3000	[129]
12	SnO_2-CuO-G	Hydrothermal	2490; 0.1 C	584/30; 0.1 C	-	[65]
13	SnO_2/NiO/C	Forcespinning and thermal treatment	1885; 100	677/100; 100	-	[130]
14	SnO_2-Co_3O_4-C	Hydrothermal, ball milling		842/300; 200	596.1; 1000	[131]
15	SnO_2@MnO_2@C	Redox	1378; 100	644.5/200; 100	434.2; 1000	[132]
16	SnO_2@MnO_2@Gaphite	Ball milling, hydrothermal	-	814.8/1000; 1000	522.2; 5000	[133]

Electrochemical performance of ZnO and carbon derivatives based ternary composites

ZnO is an electrode material with a promising theoretical capacity of 978 mAh g^{-1} towards LIBs. ZnO has a band gap of 3.37 eV along with exciting properties such as good electron mobility, photoelectric response, exciton binding energy of 60 meV, chemical and thermal stability towards many applications [134]. The general electrochemical mechanism of ZnO electrode for LIBs is presented in Equations (4) and (5).

$$ZnO + 2Li^+ + 2e^- \leftrightarrow Zn + Li_2O \quad (4)$$

$$Zn + Li^+ + e^- \leftrightarrow LiZn \quad (5)$$

ZnO undergoes a conversion reaction (Equation 1) and, in addition, more Li^+ ions can be captured by alloying-dealloying reaction (Equation 2). The materials which undergo both conversion and alloying-dealloying mechanisms are capable of delivering higher discharge capacity compared to those involving either one of the reaction mechanisms. Both reactions are reversible [135]. Besides, ZnO has several limitations, such as capacity fading issues upon cycling, low-rate capability and slow reaction kinetics [136]. There is a large volume change during discharge-charge cycling and accompanied by aggregation. Moreover, a thin layer forms at the first cycle due to the volume variation of ZnO. To achieve high specific capacity and structural stability, highly conductive electrode materials are necessary [137]. Different hierarchical architectures of nano-scaled particles could greatly increase electrochemical performance. Binary and ternary composites provide more contact area for easy transportation of ions and decrease the degradation during the cycling process. Carbon derivatives alleviate the volume expansion issues [138]. ZnO-based CDTMOs electrode materials could extend the lifetime of the battery by shortening the Li ions transportation path.

Ma *et al.* [29] fabricated the NiO-ZnO/rGO composite by annealing and ultrasonic agitation. NiO--ZnO nanoflakes were homogeneously dispersed on rGO sheets. This anode exhibited 1017 mAh g^{-1} / / 200 cycles at 100 mA $g^{-1,}$ and a higher current density of 2000 mA g^{-1} delivered 185 mAh g^{-1}. This composite is a very good example of achieving higher rate performance by shortening the diffusion of Li^+ during redox reactions.

In another work on the same composite by Huang *et al.* [139], a ternary composite of ZnO-NiO 3D flower-like mesoporous structure on graphene was developed by the hydrothermal method. This ternary composite demonstrated a higher discharge capacity of 452.7 mAh g^{-1} at a current density of 300 mA g^{-1} after 50 cycles and maintained the coulombic efficiency of 99 %. This unique structure improved the Li storage space for feasible transportation and increased the conductivity.

He *et al.* [140] developed mesoporous foldable ZnO/GeO_x/C ternary composite nanofibers with the proper distribution of GeO_x and ZnO. Due to the high surface area (532.56 $m^{-2}g^{-1}$) and mesoporous structure, carbon nanofibers exhibited the electrochemical discharge capacity of 1000 mAh g^{-1} at a current density of 0.2 A g^{-1}.

Xiaoli *et al.* [66] worked on the core-shell structure of a metal organic framework for the hybrid anode composite ZnO/$ZnCo_2O_4$/C material synthesized through a hydrothermal route. Abundant active sites created by the core-shell structure for the electrolyte penetration increase the contact area of electrode-electrolyte interfaces. This ternary composite exhibited 669 mAh g^{-1} specific capacity at 0.5 mA g^{-1} current density after 250 cycles and maintained a high discharge capacity of 715 mAh g^{-1} at 1.6 A g^{-1} current density.

Ma *et al.* [141] fabricated the hierarchical hollow structure of ZnO/$ZnFe_2O_4$/N-doped C micro polyhedrons through the self-sacrificial template method followed by calcination. N-doped carbon matrix increased the conductivity and the unique hollow structure exhibited a large discharge

capacity of 1000 mAh g^{-1}/100 cycles at 200 mA g^{-1} current density, conserving a very high capacity of 620 mAh g^{-1} after 1000 cycles.

Zhao *et al.* [142] analyzed the composite ZnO/TiO_2/C of nanofibers structures prepared by electrospinning. This composite displayed the highest specific capacity of 912 mAh g^{-1} at a current density of 100 mA g^{-1} even after 500 cycles and maintained a stable reversible capacity 294 mAh g^{-1} at 1000 mA g^{-1}. Equal molar percentages of Zn/Ti (1:1) attributed to the synergistic effect of C and interface among ZnO and TiO_2. Usually, core-shell structures of the metal-organic framework are composed of organic components with inorganic moieties bonded with covalent or other interactions capable of creating a novel huge porous structure with a very large surface area. Nitrogen, sulfur or phosphor-doped carbon compounds increased the conductivity further, increase the Li storage sites, and improve electrode/electrolyte wettability compared to undoped carbon compounds.

Table 7. *Electrochemical performance of the CDTMOs associated with ZnO*

No.	Ternary composites	Synthesis methods	Initial discharge capacity, mAh g^{-1}; Current density, mA g^{-1}	Specific capacity, mAh g^{-1} / cycles; Current density, mA g^{-1}	Rate capability, mAh g^{-1}; Current density, mA g^{-1}	Ref.
1	ZnO-NiO/rGO	Annealing and ultrasonication	1393; 100	1017/200; 100	185; 2000	[29]
2	ZnO-NiO @rGO	Hydrothermal	1205; 300	452.7/50; 300	-	[139]
2	ZnO/GeO_x/C	Electrospinning	-	464/500; 1000	-	[140]
3	ZnO/$ZnCo_2O_4$/C	Hydrothermal	1278; 0.5	669/250; 0.5	715; 1600	[66]
4	ZnO/$ZnFe_2O_4$/N-doped C	Template method	1801; 100	1000/100; 200	620; 2000	[141]
5	ZnO/TiO_2/C	Electrospinning	931; 100	912/500; 100	294; 1000	[142]

As per the listed ternary composites in Table 7, the metal-organic framework of ZnO/$ZnFe_2O_4$/N-doped C hollow structure exhibited remarkable cyclic capacity and rate capability due to hierarchical hollow structure, a synergistic effect between the two active components and N-doped carbon matrix.

Electrochemical performance of MoO_3 and carbon derivatives based ternary composites

Molybdenum is a transition refractory metal and a promising battery electrode material due to low thermal expansion, high melting point, and good electrical and thermal conductivity. Therefore it can sustain higher temperatures and possess wear resistance. Compared to orthorhombic α-MoO_3 and monoclinic β-MoO_3 polymorphs, metastable h-MoO_3 is more stable. h-MoO_3 is composed of an anisotropic zigzag pattern. The general electrochemical reaction mechanism of MoO_3 for LIBs is presented in Equations (6) and (7).

$$MoO_3 + xLi^+ + xe^- \rightarrow Li_xMoO_3 \quad (6)$$

$$Li_xMoO_3 + (6-x)Li^+ + (6-x)e^- \leftrightarrow Mo + 3Li_2O \quad (7)$$

Equations explain the intercalation and de-intercalation of Li-ions into the MoO_3 matrix. The oxidation process of intercalating Li-ions into layered MoO_3 takes place and the reverse mechanism occurs during the de-intercalation process. Initially, a thin layer called solid electrolyte interface (SEI) takes place and later forms bulk Li_xMoO_3 to form Mo metal and Li_2O composites by conversion mechanism [143,144].

Zeng *et al.* [86] have fabricated the CNT/SiO_2/MoO_3 composite of cactus-like structure synthesized through in-situ carbonization of the self-assembly method. CNT/SiO_2/MoO_3 ternary composite delivered a specific capacity of 700 mAh g^{-1}/500 cycles at 1000 mA g^{-1}. Here higher capacity is attributed to the alleviation of strain by the unique structure contributed by each component.

Deng *et al.* [145] anchored SnO_2-MoO_3 NPs to CNTs through hydrothermal and ball-grinding methods. SnO_2-MoO_3/CNT exhibited a specific capacity of 1372.2 mAh g^{-1}/280 cycles at 200 mA g^{-1}. The SnO_2-MoO_3-CNT ternary composite displayed excellent cyclic capacity and rate capability.

Cao *et al.* [146] have decorated the ultrasmall WO_2 NPs for the carbon-coated MoO_3 nanorods by hydrothermal method. WO_2 provided a high conductivity of 2.2 mΩ cm at room temperatures. MoO_3/WO_2@C composite delivered a reversible capacity of 815 mAh g^{-1}/100 cycles at 0.05 C and an outstanding cyclic capacity of 80 mAh g^{-1} after 5000 cycles at 1 C-rate.

Teng *et al.* [147] fabricated MoO_3-NiO/graphene through a one-pot synthesis method. In this paper, MoO_3 nanosheets and NiO NPs, anchored homogeneously on the graphene layers, contributed to achieving a short diffusion path and reducing the volume expansion. MoO_3-NiO/graphene exhibited a higher discharge capacity of 946.9 mAh g^{-1}/ 180 cycles at 1000 mA g^{-1}.

Table 8. *Electrochemical performance of the CDTMOs associated with MoO3*

No.	Ternary composites	Synthesis methods	Initial discharge capacity, mAh g^{-1}; Current density, mA g^{-1} or C-rate	Specific capacity, mAh g^{-1} / cycles; Current density, mA g^{-1} or C-rate	Rate capability, mAh g^{-1}; Current density, mA g^{-1} or C-rate	Ref.
1	MoO_3/SiO_2/CNT	Carbonization	1090; 100	450/150; 100	320; 5000	[86]
2	MoO_3-SnO_2-CNT	Hydrothermal and ball milling	-	1372.2/280; 200	743.6; 5000	[145]
3	MoO_3/WO_2@C	Hydrothermal	869; 0.05 C	815/100; 0.05 C-rate	80; 1 C-rate	[146]
4	MoO_3-NiO/graphene	One-pot method	-	1164/50; 100	946.9; 1000	[147]

The highest remarkable cyclic capacity and rate capability have been exhibited by the MoO_3-NiO/graphene ternary composite impacted by low volume expansion, fast rection rate and short diffusion path; among the listed ternary composites based on MoO_3 (Table 8).

Electrochemical performance of SiO_x and carbon derivatives based ternary composites

Silicon (SiO_x) is the active component for storing the high capacity towards LIBs. Si is primarily desirable for EV applications because of its high density and theoretical volumetric capacity higher than graphite. Si anodes exhibited a higher theoretical capacity of 3579 mAh g^{-1}. Si might show four separate phases, $Li_{12}Si_7$, Li_7Si_3, $Li_{13}Si_4$, and $Li_{22}Si_5$, at high temperature (415 °C), compared to the Si lithiation process which has two transition stages at room temperature.

$$SiO_x + 2xLi^+ + 2xe^- \rightarrow xLi_2O + Si \quad (8)$$

$$SiO_x + xLi^+ + xe^- \rightarrow 0.25xLi_4SiO_4 + (1- 0.25x)Si \quad (9)$$

$$SiO_x + 0.4xLi^+ + 0.4xe^- \rightarrow 0.25xLi_2Si_2O_5 + (1 - 0.4x)Si \quad (10)$$

In the first lithiation process (Equations 8, 9 and 10), a high concentration of Li atoms is accumulated in the Li_xSi/Si. Importantly, only the amorphous Si-Li phase could be formed as per the concern of equilibrium phases, but it is kinetically hindered [148,149]. Despite the concerted efforts, the inherent drawbacks of silicon for usage as an anode remain unaddressed for commercial implementation. First, silicon is a bad conductor of electricity. A low-cost carbon matrix solution could easily fix this. This strategy has been proved in several articles. This way helps to achieve electrical conductivity. Reducing the silicon size to nanoscale shortens lithium-ion diffusion distance.

Gu *et al.* [150] reported SiO_x@SnO_2@C ternary composite of microspheres by hydrothermal approach. This unique architecture exhibited a 796 mAh g^{-1} specific capacity at 1000 mA g^{-1} after 300 cycles and achieved a high capacity of 515 mAh g^{-1} at the higher current density of 4000 mA g^{-1}.

Hu *et al.* [151] fabricated Fe_3O_4@SiO_2@rGO ternary composite anode material by chemical etching. This composite displayed a 514 mAh g^{-1} specific capacity at the higher current density of

5000 mA g^{-1} even after 1000 cycles. Porous SiO_2 shell and rGO nanosheets enable the pseudocapacitance for obtaining fast discharge-charge cycles.

Wang *et al.* [80] prepared promising anode material composed of SiO/Ni/graphite through two-step ball-milling method. This ternary hierarchical composite fixes its volume expansion issue by increasing the utilization efficiency of SiO. It exhibited a higher initial discharge capacity of 1331.5 mAh g^{-1} and maintained a 522 mAh g^{-1} stable capacity even after 50 cycles at a higher current rate of 1000 mA g^{-1}.

Tan *et al.* [152] fabricated SiO_x@TiO_2/C fibers composite by electrospinning method. This combination provided mechanical stability to enhance the conductivity. It exhibited a stable charge capacity of 855 mAh g^{-1} at 100 mA g^{-1} current density even after 100 cycles and maintained 640.4 mAh g^{-1} specific capacity at 1000 mA g^{-1} even after 100 cycles.

Jiang *et al.* [153] developed TiO_2/SiO_2/C film through an electrospinning approach. It exhibited a 380 mAh g^{-1} specific capacity at 200 mA g^{-1} current density after 700 cycles. This combination of current collectors also lowers the electrode's weight and cost.

Table 9. *Electrochemical performance of the CDTMOs associated with SiOx*

No.	Ternary composites	Synthesis methods	Initial discharge capacity, mAh g^{-1}; Current density, mA g^{-1}	Specific capacity, mAh g^{-1} / cycles; Current density, mA g^{-1}	Rate capability, mAh g^{-1}; Current density, mA g^{-1}	Ref.
1	SiO_x@SnO_2@C	Hydrothermal	2186, 100	796/300, 1000	515, 4000	[150]
2	Fe_3O_4@SiO_2@rGO	Chemical -itching	1630, 100	901/150, 100	514/1000, 5000	[151]
3	SiO/Ni/graphite	Ball milling	1332, 100	522/50, 1000	-	[80]
4	SiO @TiO_2/C	Electrospinning	1125, 100	855/100, 100	640.4/200, 1000	[152]
5	TiO_2/SiO_2/C	Electrospinning	-	380.1/700, 200	115.5, 8000	[153]

Superior cyclic capacity and rate capability were exhibited by the Fe_3O_4@SiO_2@rGO and SiO_x@SnO_2@C ternary composite by increasing the conductivity and tuning the structures of ternary composites among the cited ternary composites based on SiO_x (Table 9).

Electrochemical performance of other MOs and carbon derivatives based ternary composites

Other metal oxides of cobalt, titanium, nickel, copper, iron, manganese and other metal oxides-oriented graphene derivatives incorporated ternary composites are discussed in this section. The flexible matrix can be made with manganese oxide Mn_3O_4. It is a good candidate for the accommodation of the volume change, low cost and can exhibit 900 mAh g^{-1} specific capacity. MnO_2 introduces a high theoretical capacity of 1233 mAh g^{-1} [154]. Co_3O_4 exhibits a high theoretical capacity of 890 mAh g^{-1} but also possesses a few disadvantages, including toxicity, high cost, and high operating voltage (2.2 to 2.4 V *vs.* Li^+/Li) [155]. NiO is a low-cost, abundant, environmentally benign electrode material with a theoretical capacity of 718 mAh g^{-1} [156]. TiO_2 and Fe_2O_3 electrode materials are popular due to their low cost and high discharge-charge capacities [157]. Titanium oxide stores the Li efficiently through insertion reaction and displays different crystal structures, including rutile, anatase, TiO_2 (bronze) and brookite [158]. CuO can store the high reversible capacity of 716 mAh g^{-1}, structural collapsing due to single metal oxide [159]. These single metal oxides suffer from large volume changes during redox reactions. Combining with other metal oxides and carbon derivatives helps overcome the pulverization issues. Here we discussed the few electrode materials for CDTMOs.

Zuniga *et al.* [160] developed α-Fe_2O_3/TiO_2/carbon composite fibers anode materials through centrifugal spinning and thermal processing. The α-Fe_2O_3/TiO_2/C composite fibers exhibited a 340 mAh g^{-1} after 100 cycles at a current density of 100 mA g^{-1} compared to TiO_2/C and Fe_2O_3/C composite electrodes due to the high diffusion kinetics and structural stability of TiO_2 and Fe_2O_3.

Kaprans *et al.* [161] have electrophoretically deposited α-Fe_2O_3/TiO_2/rGO. Formed films were between 2-6 µm thick. They have performed comparative study between α-Fe_2O_3/TiO_2/rGO and TiO_2/rGO and composites. Proved that the composite α-Fe_2O_3/TiO_2/rGO displayed the specific discharge capacity of 790 mAh g^{-1} after 150 cycles at the current density of 100 mA g^{-1}, coulombic efficiency of 66 % and exhibited 390 mAh g^{-1}specific capacity at 500 mA g^{-1} compared to other compounds.

Wang *et al.* [162] fabricated a Co_3O_4/TiO_2/carbon composite using natural cellulose substrate through a sol-gel route to form a thin TiO_2 gel layer coating and hydrothermal method for the uniform deposition of Co_3O_4 particles. This hierarchical nanostructure exhibited a porous structure with a high surface area, providing enough ions transportation path. The inner carbon nanofiber acts as a buffer layer, helps to relieve the strain during volume expansion and improves the efficiency of electrons movement. This composite delivered the initial discharge capacity of 1239 mAh g^{-1} at a current density of 100 mA g^{-1} after 200 cycles, displayed a discharge capacity of 764 mAh $g^{-1}$and at a higher rate of 1 A g^{-1} exhibited a 348 mAh g^{-1}. Zhang *et al.* [163] have designed CoO/CuO/rGO ternary nanocomposites synthesized through a facile cost-effective method. Anode material, the CoO/CuO/rGO ternary composite, delivered a stable capacity of 1364.6 mAh g^{-1} at a current density of 0.2 A g^{-1}/ 100 cycles. It retained 423.5 mAh g^{-1} even after 100 cycles at an increased rate capacity of 2000 mA g^{-1}.

Wu *et al.* [164] designed Co_3O_4/NiO/C core/shell nanowire arrays by hydrothermal synthesis, chemical bath deposition and annealing carbonation methods. Porous Co_3O_4 acts as a core backbone on the developed NiO nanoflakes. Ternary composite exhibited 1050 mAh g^{-1}discharge capacity after 50 cycles at 0.5 C and maintained 769 mAh g^{-1} specific capacity at the higher rate of 2 C compared to individual Co_3O_4 and NiO metal oxides due to the lowering of the polarization.

Table 10. *Electrochemical performance of the CDTMOs associated with other metal oxides*

No.	Ternary composites	Synthesis methods	Initial discharge capacity, mAh g^{-1}; Current density, mA g^{-1} or C-rate	Specific capacity, mAh g^{-1} / cycles; Current density, mA g^{-1} or C-rate	Rate capability, Ah g^{-1}; Current density, mA g^{-1} or C-rate	Ref.
1	αFe_2O_3/TiO_2/C	Spinning and thermal processing	1832	340/100; 100	200, 500	[160]
2	αFe_2O_3/TiO_2/rGO	Electrophoretically deposited	765; 50	790/150; 100	390, 500	[161]
3	Co_3O_4/TiO_2/C	Sol-gel and hydrothermal	1239; 100	764/200; 100	348, 1000	[162]
4	CoO/CuO/rGO	Facile method	1732.4; 200	1364.6/100; 200	423.5, 2000	[163]
5	Co_3O_4/NiO/C	Hydrothermal, chemical bath deposition and carbonization	1426; 0.5 C	1053/50; 0.5 C	769, 2 C	[164]

According to Table 10, the ternary composite of Co_3O_4/NiO/C displayed higher cyclic capacity as well as rate capability ascribed due to the core/shell structure of nanowire arrays. This novel architecture succeeded in lowering the polarization of the electrode.

Capacity fading mechanism in ternary composites

Li-ion battery capacity decreases gradually during cycling. Capacity fading occurs due to many different reaction mechanisms. The reasons behind the capacity fading mechanism in the available literature towards LIBs are mainly due to:

1. The pulverization of the electrode materials happens due to increasing the internal resistance during the cycling process, which causes the barrier to the flow of charge carriers by current collectors. Current collectors undergo passive film formation and corrosion.
2. Irreversible redox reactions forming the solid electrolyte interface, self-discharge, and creating the passive layer on the electrodes.

3. Many reaction mechanisms and the formation of unnecessary side reactions and undesirable phase changes.
4. Decomposition of the electrolyte due to the increasing Li content. Overcharging also induces Li deposition on the electrode.

Balamurugan *et al.* [165] reported the capacity fading mechanism $NiFe_2O_4/SiO_2$ aerogel anode prepared via the sol-gel method. They loaded a small amount of Li_2O to increase electrical conductivity. The initial discharge capacity of 930 mAh g^{-1} gradually faded to 370 mAh g^{-1} at the 50th cycle of discharging. They have explored the capacity fading mechanism by ex-situ X-ray photoelectron spectroscopy (XPS) technique to identify the changing in the oxidation states during dischargeing/charging process. Capacity fading began from the accumulation of irreversible Li_xSiO_y. It causes the loss of active Li. Cell resistance was increased during the 1st cycle to the 10th discharge cycle.

Ziv *et al.* [166] have investigated the reasons for capacity fading in Li-ion cells. They have examined the cathode materials such as $LiMn_{0.8}Fe_{0.2}PO_4$ (LMFP), $LiNi_{0.5}Mn_{1.5}O_4$ (LMNO), $Li[Li_xNi_yCo_zMn_{1-x-y-z}]O_2$, Li-rich layered oxides (HC-MNC) and Li-rich layered oxides (HC-MNC). Analysis of dissembled electrodes revealed that the main cause of capacity fading in Li-ion battery full cells is the loss of active lithium ions due to parasitic side reactions.

Kim *et al.* [167] reported the fading mechanism of $LiNiCo_{0.1}Mn_{0.1}O_2$ in Li-ion cells. In this work, they tested the pouch cell after 1, 100, 200 and 300 cycles. 16.3 % of the capacity was faded and the loss of the lithium source was confirmed by XRD. Mechanical failure was confirmed by FE-SEM.

Conclusion and future perspectives

We provided a brief review of SnO_2, ZnO, MoO_3, SiO_x and other important metal oxides with carbon derivatives based ternary composites for the lithium-ion battery application. We started with a discussion of various synthesis methods for synthesizing metal oxides, carbonaceous materials, and their combinations. Carbonaceous materials include carbon, graphite, graphene oxide (GO), reduced graphene oxide (rGO), and carbon nanotubes (CNTs). They have gained attention for their enhanced electrochemical performance by incorporating metal oxides. We reviewed the importance of various synthesis methods of electrode materials by tailoring the experimental conditions, such as operating duration and temperature and choosing additional agents for the surface modification to explore the different shapes and sizes. We have discussed the reaction mechanisms of SnO_2, ZnO, MoO_3, and SiO_x metal oxides during the intercalation-deintercalation of Li-ion. Then we discussed the SnO_2, ZnO, MoO_3, SiO_x and carbon derivatives oriented ternary composites synthesis methodology, morphology, and electrochemical performance towards LIBs. Ternary composites alleviate many drawbacks, such as initial capacity fading and volume expansion, with the synergistic effect of taking out the individual compound's advantages and enhancement of rate performance by carbonaceous additives.

Surveying the SnO_2-based ternary electrode materials revealed that the many drawbacks, including pulverization, and capacity fading of the individual SnO_2, can be greatly alleviated by the preparation of composite materials, especially with carbonaceous materials. Composite materials incorporating carbonaceous materials tend to increase the conductivity of electrode materials and tailor the surface morphology, which can greatly impact the cyclic stability and rate capability.

ZnO is good electrode material with few drawbacks, including capacity fading through slow reaction kinetics resulting in poor rate capability. Carbon derivatives incorporated ZnO-based ternary composites resolved the individual drawbacks of ZnO by the synergistic effects between the compounds. Correlation among the individual metal oxides and carbon derivatives plays a premier

role in improving the overall performance electrochemically. ZnO-based ternary composites provided a large interaction area, more reaction area, short diffusion kinetics and, reduced volume expansion, different synthesis methods to explore the various structures of ZnO-based ternary composites. In the reaction mechanism, reversible alloying-dealloying reactions have benefitted more in increasing the coulombic efficiency compared to the conversion mechanism.

MoO_3-based composite ternary electrode materials have become potential electrode materials for LIBs due to the capability of storing a large amount of Li. As per the literature, h-MoO_3 has a more beneficial polymorph version. Remarkable electrochemical performance could be achievable by combining the other MOs and carbonaceous materials.

SiO_x is a very good alloying anode material for high energy density LIBs. High concentrations of Li atoms reversibly can incorporate with SiO_x. SiO_x anode fails to provide good cycle life. Composite materials of silicon can become good candidates for LIBs. SiO_x with Fe_3O_4 and rGO ternary composite exhibited superior cyclic and rate performance.

Developing promising novel electrode materials by engineering their structure and combining them with carbonaceous materials could achieve superior electrochemical performance for LIBs. The relationship between the active materials, binders and electrolytic additives will impact the SEI layer and improve the coulombic efficiency, rate capability and cyclic performance. Strategies to develop the carbonaceous materials incorporated metal oxides to form ternary composites with heterostructures for the LIBs electrode materials have been studied widely in the perception of practical usage.

References

[1] G. E. Blomgren, The development and future of lithium-ion batteries, *Journal of the Electrochemical Society* **164** (2016) A5019. https://doi.org/10.1149/2.0251701jes

[2] R. Tian, G. Liu, H. Liu, L. Zhang, X. Gu, Y. Guo, H. Wang, Very high power and superior rate capability $LiFePO_4$ nanorods hydrothermally synthesized using tetraglycol as surfactant, *RSC Advances* **5** (2015) 1859-1866. https://doi.org/10.1039/C4RA09776A

[3] C. Liu, U. Burghaus, F. Besenbacher, Z. L. Wang, Preparation and characterization of nanomaterials for sustainable energy production, *ACS Nano* **4** (2010) 5517-5526. http://doi.org/10.1021/nn102420c

[4] B. Goodenough, K. S. Park, The Li-ion rechargeable battery: a perspective, *Journal of the American Chemical Society* **135** (2013) 1167-1176. https://doi.org/10.1021/ja3091438

[5] S. Wu, R. Xu, M. Lu, R. Ge, J. Iocozzia, C. Han, B. Jiang, Graphene-containing nanomaterials for lithium-ion batteries, *Advanced Energy Materials* **5** (2015) 1500400. https://doi.org/10.1002/aenm.201500400

[6] L. Liu, F. Xie, J. Lyu, T. Zhao, T. Li, B. G. Choi, Tin-based anode materials with well-designed architectures for next-generation lithium-ion batteries, *Journal of Power Sources* **321** (2016) 11-35. https://doi.org/10.1016/j.jpowsour.2016.04.105

[7] N. Mahne, S. E. Renfrew, B. D. McCloskey, S. A. Freunberger, Electrochemical oxidation of lithium carbonate generates singlet oxygen, *Angewandte Chemie International Edition* **57** (2018) 5529-5533. https://doi.org/10.1002/anie.201802277

[8] M. V. Reddy, G. V. Subba Rao, B. V. R. Chowdari, Metal oxides and oxysalts as anode materials for Li-ion batteries, *Chemical reviews* **113** (2013) 5364-5457. https://doi.org/10.1021/cr3001884

[9] S. Alagar, C. Karuppiah, R. Madhuvilakku, S. Piraman, Temperature-controlled synthesis of Li-and Mn-rich $Li_{1.2}Mn_{0.54}Ni_{0.13}Co_{0.13}O_2$ hollow nano/ sub-microsphere electrodes for high-

performance lithium-ion battery, *ACS omega* **4** (2019) 20285-20296. https://doi.org/10.1021/acsomega.9b02766

[10] C. Ai, M. Yin, C. Wang, J. Sun, Synthesis and characterization of spinel type $ZnCo_2O_4$ as a novel anode material for lithium-ion batteries, *Journal of materials science* **39** (2004) 1077-1079. http://doi.org/10.1023/b:jmsc.0000012948.27433.83

[11] H. Aghamohammadi, R. Eslami-Farsani, E. Castillo-Martinez, Recent trends in the development of MXenes and MXene-based composites as anode materials for Li-ion batteries, *Journal of Energy Storage* **47** (2022) 103572. https://doi.org/10.1016/j.est.2021.103572

[12] Q. Shi, J. Zhou, S. Ullah, X. Yang, K. Tokarska, B. Trzebicka, M. H. Rummeli, A Review of Recent Developments in Si/C Composite Materials for Li-ion Batteries, Energy Storage Materials, *Energy Storage Materials* **3** (2021) 735-754. https://doi.org/10.1016/j.ensm.2020.10.026

[13] F. Wu, J. Maier, Y. Yu, Guidelines and trends for next-generation rechargeable lithium and lithium-ion batteries, Chemical Society Reviews **49** (2020) 1569-1614. https://doi.org/10.1039/C7CS00863E

[14] F. Larouche, F. Tedjar, K. Amouzegar, G. Houlachi, P. Bouchard, G. P. Demopoulos, K. Zaghib Progress and Status of Hydrometallurgical and Direct Recycling of Li-Ion Batteries and Beyond *Materials* **13** (2020) 801. https://doi.org/10.3390/ma13030801

[15] F. Belliard, J. T. S. Irvine, Electrochemical performance of ball-milled ZnO-SnO_2 systems as anodes in lithium-ion battery, *Journal of Power Sources* **97** (2001) 219–222. https://doi.org/10.1016/S0378-7753(01)00544-4

[16] G. Yuan, G. Wang, H. Wang, J. Bai, Synthesis and electrochemical investigation of radial ZnO microparticles as anode materials for lithium-ion batteries, *Ionics* **21** (2015) 365–371. https://doi.org/10.1007/s11581-014-1188-y

[17] V. Aravindan, K. B. Jinesh, R. R. Prabhakar, V. S. Kale, S. Madhavi, Atomic layer deposited (ALD) SnO_2 anodes with exceptional cycleability for Li-ion batteries, *Nano Energy* **2** (2013) 720–725. https://doi.org/10.1016/j.nanoen.2012.12.007

[18] K. Y. K. Yamazaki, K. K. K. Kurihara, T. Y. T. Yamaguchi, Novel proximity effect including pattern-dependent resist development in electron beam nanolithography, *Japanese journal of applied physics* **36** (1997) 7552. http://doi.org/10.1143/JJAP.36.7552

[19] K. Okuyama, I. W. Lenggoro, Preparation of nanoparticles via spray route, *Chemical engineering science* **58** (2003) 537-547. https://doi.org/10.1016/S0009-2509(02)00578-X

[20] J. Liu, S. H. He, J. P. Wang, High-yield gas-phase condensation synthesis of nanoparticles to enable a wide array of applications, *ACS Applied Nano Materials* **3** (2020) 7942-7949. https://doi.org/10.1021/acsanm.0c01400

[21] A. Hassani, M. Karaca, S. Karaca, A. Khataee, O. Açişli, Preparation of magnetite nanoparticles by high-energy planetary ball mill and its application for ciprofloxacin degradation through heterogeneous Fenton process, *Journal of environmental management* **211** (2018) 53-62. https://doi.org/10.1016/j.jenvman.2018.01.014

[22] S. Kurajica, I. Minga, M. Gulis, V. Mandic, I. Simcic, High surface area ceria nanoparticles via hydrothermal synthesis experiment design, *Journal of Nanomaterials* (2016) Article ID 7274949 1-8. https://doi.org/10.1155/2016/7274949

[23] K. Petcharoen, A. Sirivat, Synthesis and characterization of magnetite nanoparticles via the chemical co-precipitation method, *Materials Science and Engineering: B* **177** (2012) 421-427. https://doi.org/10.1016/j.mseb.2012.01.003

[24] V. Pavitra, R. Harini, R. Viswanatha, B. M. Praveen, G. Nagaraju, Sonochemical synthesis of SnO_2-CuO nanocomposite: diverse applications on Li-ion battery, electrochemical sensing

and photocatalytic activity, *Journal of Materials Science: Materials in Electronics* **31** (2020) 8737-8749. https://doi.org/10.1007/s10854-020-03408-5

[25] M. Niederberger, Nonaqueous sol–gel routes to metal oxide nanoparticles, *Accounts of chemical research* **40** (2007) 793-800. https://doi.org/10.1021/ar600035e

[26] U. S. Mohanty, Electrodeposition: a versatile and inexpensive tool for the synthesis of nanoparticles, nanorods, nanowires, and nanoclusters of metals, *Journal of applied electrochemistry* **41** (2011) 257-70. https://doi.org/10.1007/s10800-010-0234-3

[27] Y. R. Parauha, V. Sahu, S. J. Dhoble, Prospective of combustion method for preparation of nanomaterials: A challenge, *Materials Science and Engineering: B* **267** (2021) 115054. https://doi.org/10.1016/j.mseb.2021.115054

[28] F. Yao, D. T. Pham, Y. H. Lee, Carbon-based materials for lithium-ion batteries, electrochemical capacitors, and their hybrid devices, *ChemSusChem* **8** (2015) 2284-2311. https://doi.org/10.1002/cssc.201403490

[29] L. Ma, X. Y. Pei, D. C. Mo, S. S. Lyu, Y. X. Fu, Fabrication of NiO-ZnO/RGO composite as an anode material for lithium-ion batteries, *Ceramics International* **44** (2018) 22664-22670. https://doi.org/10.1016/j.ceramint.2018.09.044

[30] L. Khandare, D. J. Late, MoO_3-rGO nanocomposites for electrochemical energy storage, *Applied Surface Science* **418** (2017) 2-8. https://doi.org/10.1016/j.apsusc.2016.11.199

[31] H. He, J. Klinowski, M. Forster, A. Lerf, A new structural model for graphite oxide, *Chemical physics letters* **287** (1998) 53-56. https://doi.org/10.1016/S0009-2614(98)00144-4

[32] A. K. Geim, K. S. Novoselov, The rise of graphene, *Nature Materials **6** (2007) 183-191.* https://doi.org/10.1038/nmat1849

[33] S. Iijima, Helical microtubules of graphitic carbon, *Nature* **354** (1991) 56-58. https://doi.org/10.1038/354056a0

[34] S. J. Tans, M. H. Devoret, H. Dai, A. Thess, R. E. Smalley, Individual single-wall carbon nanotubes as quantum wires, *Nature* **386** (1997) 474-477. https://doi.org/10.1038/386474a0

[35] M. F. Yu, O. Lourie, M. J. Dyer, K. Moloni, T. F. Kelly, R. S. Ruoff, Strength and breaking mechanism of multiwalled carbon nanotubes under tensile load, *Science* **287** (2000) 637-640. http://doi/10.1126/science.287.5453.63

[36] V. A. NebolSin, V. Galstyan, Y. E. Silina, Graphene oxide and its chemical nature: Multi-stage interactions between the oxygen and graphene, *Surfaces and Interfaces* **21** (2020) 100763. https://doi.org/10.1016/j.surfin.2020.100763

[37] S. William, J. R. Hummers, R. E. Offeman, Preparation of graphitic oxide, *Journal of the American Chemical Society* **80** (1958) 1339-1339. https://doi.org/10.1021/ja01539a017

[38] M. Fathy, A. Gomaa, F. A Taher, M. M. El-Fass, Optimizing the preparation parameters of GO and rGO for large-scale production, *Journal of Materials Science* **51** (2016) 5664-5675. https://doi.org/10.1007/s10853-016-9869-8

[39] S. Muralikrishna, B. Kishore, H. Nagabhushana, D. Suresh, S. C. Sharma, and G. Nagaraju. One pot green synthesis of $MnCO_3$–rGO composite hybrid superstructure: application to lithium-ion battery and biosensor, *New Journal of Chemistry* **41** (2017) 12854-12865. http://doi.org/10.1039/c7nj01781b

[40] D. Suresh, P. C. Nethravathi, H. Nagabhushana, Spinach assisted green reduction of graphene oxide and its antioxidant and dye absorption properties, *Ceramics International* **41** (2015) 4810-4813. https://doi.org/10.1016/j.ceramint.2014.12.036

[41] J. Shi, X. Jiang, B. Ban, J. Li, J. Chen, Carbon nanotubes-enhanced lithium storage capacity of recovered silicon/carbon anodes produced from solar-grade silicon kerf scrap, Electrochimica Acta, **381** (2021) 138269. https://doi.org/10.1016/j.electacta.2021.138269

[42] Y. Zhang, Y. Wei, H. Li, Y. Zhao, F. Yin, X. Wang, Simple fabrication of free-standing ZnO/graphene/carbon nanotube composite anode for lithium-ion batteries, *Materials Letters* **184** (2016) 235-238. https://doi.org/10.1016/j.matlet.2016.08.017

[43] V. Thirumal, R. Yuvakkumar, P. S. Kumar, G. Ravi, Facile single-step synthesis of MXene@ CNTs hybrid nanocomposite by CVD method to remove hazardous pollutants, *Chemosphere* **286** (2022) 131733. https://doi.org/10.1016/j.chemosphere.2021.131733

[44] D. Tang, L. Sun, J. Zhou, W. Zhou, S. Xie, Two possible emission mechanisms involved in the arc discharge method of carbon nanotube preparation, *Carbon* **43** (2005) 2812-2816. https://doi.org/10.1016/j.carbon.2005.05.034

[45] J. Chrzanowska, J. Hoffman, A. Małolepszy, Synthesis of carbon nanotubes by the laser ablation method: Effect of laser wavelength, *physica status solidi (b)* **252** (2015) 1860-1867. https://doi.org/10.1002/pssb.201451614

[46] J. S. Chen, Y. L. Cheah, Y. T. Chen, N. Jayaprakash, S. Madhavi, Y. H. Yang, & X. W. Lou, SnO_2 Nanoparticles with Controlled Carbon Nanocoating as High-Capacity Anode Materials for Lithium-Ion Batteries, *The Journal of Physical Chemistry C* **113** (2009) 20504–20508. https://doi.org/10.1021/jp908244m

[47] V. Pavitra, B. M. Praveen, G. Nagaraju, R. Shashanka, Energy Storage, Photocatalytic and Electrochemical Nitrite Sensing of Ultrasound-Assisted Stable Ta_2O_5 Nanoparticles, *Topics in Catalysis* (2022) 1-14. https://doi.org/10.1007/s11244-021-01553-7

[48] V. D. Potle, S. R. Shirsath, B. A. Bhanvase, V. K. Saharan, Sonochemical preparation of ternary rGO-ZnO-TiO_2 nanocomposite photocatalyst for efficient degradation of crystal violet dye, *Optik* **208** (2020) 164555. https://doi.org/10.1016/j.ijleo.2020.164555

[49] B. Raj, R. Oraon, A.K. Padhy, Simple and cost-effective sonochemical preparation of ternary NZnO–Mn_2O_3@rGO nanohybrid: a potential electrode material for supercapacitor and ammonia sensing, *Ionics* **25** (2019) 3351-3362. https://doi.org/10.1016/j.ijleo.2020.164555

[50] H. Asgar, K.M. Deen, W. Haider, Estimation of electrochemical charge storage capability of ZnO/CuO/reduced graphene oxide nanocomposites, *International Journal of Energy Research* ***44*** (2020) 1580-1593. https://doi.org/10.1002/er.4961

[51] T. P. Shende, B. A. Bhanvase, A. P. Rathod, D. V. Pinjari, Sonochemical synthesis of Graphene-Ce-TiO_2 and Graphene-Fe-TiO_2 ternary hybrid photocatalyst nanocomposite and its application in degradation of crystal violet dye, *Ultrasonics sonochemistry* **41** (2018) 582-589. https://doi.org/10.1016/j.ultsonch.2017.10.024

[52] Udayabhanu, V. Pavitra, S. C. Sharma, G. Nagaraju, *Epigallocatechin gallate* (EGCG)–assisted combustion synthesis of V_2O_5 nanoparticles for Li-ion battery, *Ionics* **26** (2020) 1203-1210. https://doi.org/10.1007/s11581-019-03326-5

[53] A. Kumar, L. Rout, L.S.K. Achary, S.K. Mohanty, P. Dash, A. combustion synthesis route for magnetically separable graphene oxide–$CuFe_2O_4$–ZnO nanocomposites with enhanced solar light-mediated photocatalytic activity, *New journal of chemistry* 41 (2017) 10568-10583.https://doi.org/10.1039/C7NJ02070H

[54] N. K. Rotte, N. Remalli, V. V. S. S. Srikanth, Simple combustion synthesis of MgO and NiO decorated graphenaceous composite, *Materials Letters* **183** (2016) 251-254. https://doi.org/10.1016/j.matlet.2016.07.112

[55] A. K. Rai, T. V. Thi, J. Gim, J. Kim, Combustion synthesis of $MgFe_2O_4$/graphene nanocomposite as a high-performance negative electrode for lithium-ion batteries, *Materials characterization* **95** (2014) 259-265. https://doi.org/10.1016/j.matchar.2014.06.024

[56] L. Kang, J. Deng, T. Liu, M. Cui, X. Zhang, P. Li, Y. Li, X. Liu, One-step solution combustion synthesis of cobalt–nickel oxides/C/Ni/CNTs nanocomposites as electrochemical capacitors

electrode materials, *Journal of Power Sources* **275** (2015) 126-135. https://doi.org/10.1016/j.jpowsour.2014.10.201

[57] R. Q. Song, A. W. Xu, B. Deng, Y. P. Fang, Novel multilamellar mesostructured molybdenum oxide nanofibers and nanobelts: synthesis and characterization, *The Journal of Physical Chemistry B* **109** (2005) 22758-22766. https://doi.org/10.1021/jp0533325

[58] S. Wang, Q. Li, W. Pu, Y. Wu, M. Yang, MoO_3-MnO_2 intergrown nanoparticle composite prepared by one-step hydrothermal synthesis as anode for lithium-ion batteries, *Journal of Alloys and Compounds* **663** (2016) 148-155. https://doi.org/10.1016/j.jallcom.2015.12.040

[59] S. M. Botsa, G. P. Naidu, M. Ravichandra, S. J. Rani, Flower like SnO_2-Fe_2O_3-rGO ternary composite as highly efficient visible light induced photocatalyst for the degradation of organic pollutants from contaminated water, *Journal of Materials Research and Technology* **9** (2020) 12461-12472. https://doi.org/10.1016/j.jmrt.2020.08.087

[60] M. Amarnath, A. Heiner, K. Gurunathan, Surface bound nanostructures of ternary r-GO/Mn_3O_4/V_2O_5 system for room temperature selectivity of hydrogen gas, *Ceramics International* **46** (2020) 7336-7345. https://doi.org/10.1016/j.ceramint.2019.11.229

[61] Y. C. Chung, A. Julistian, L. Saravanan, P. R. Chen, B. C. Xu, Hydrothermal synthesis of CuO/RuO_2/MWCNT nanocomposites with morphological variants for high efficient supercapacitors, *Catalysts* **12** (2021) 23. https://doi.org/10.3390/catal12010023

[62] G. S Kumar, S. A. Reddy, H. Maseed, N. R. Reddy, Facile hydrothermal synthesis of ternary CeO_2-SnO_2/rGO nanocomposite for supercapacitor application, *Functional Materials Letters* **13** (2020) 2051005. https://doi.org/10.1142/S1793604720510054

[63] W. Wu, Y. Zhao, J. Li, C. Wu, L. Guan, A ternary phased SnO_2-Fe_2O_3/SWCNTs nanocomposite as a high-performance anode material for lithium-ion batteries, *Journal of energy chemistry* **23** (2014) 376-382. https://doi.org/10.1016/S2095-4956(14)60160-1

[64] Y. Huang, X. Chen, K. Zhang, X. Feng, Preparation of graphene supported porous SnO_2/NiO ternary composites as high-capacity anode materials for Li-ion batteries, *Materials Letters* **161** (2015) 631-635. https://doi.org/10.1016/j.matlet.2015.09.074

[65] J. Zhao, W. Shan, X. Xia, Q. Wang, L. Xing, SnO_2-CuO/graphene nanocomposites for high performance Li-ion battery anodes, *Science China Technological Sciences* 57 (2014) 1081–1084. https://doi.org/10.1007/s11431-014-5507-3

[66] X. Ge, Z. Li, C. Wang, L. Yin, Metal–organic frameworks derived porous core/shell structured ZnO/$ZnCo_2O_4$/C hybrids as anodes for high-performance lithium-ion battery, *ACS applied materials & interfaces* **7** (2015) 26633-26642. https://doi.org/10.1021/acsami.5b08195

[67] J. Yao, Y. Gong, S. Yang, P. Xiao, Y. Zhang, K. Keyshar, $CoMoO_4$ nanoparticles anchored on reduced graphene oxide nanocomposites as anodes for long-life lithium-ion batteries, *ACS Applied Materials & Interfaces* **6** (2014) 20414-20422. https://doi.org/10.1021/am505983m

[68] J. W. Lee, S. D. Seo, D. W. Kim, Hierarchical $Zn_{1.67}$ $Mn_{1.33}O_4$/graphene nanoaggregates as new anode material for lithium-ion batteries, *International Journal of Energy Research* **43** (2019) 1735-1746. https://doi.org/10.1002/er.4381

[69] N. Sebastian, W. C. Yu, Y. C. Hu, D. Balram, Y. H. Yu, Sonochemical synthesis of iron-graphene oxide/honeycomb-like ZnO ternary nanohybrids for sensitive electrochemical detection of antipsychotic drug chlorpromazine, *Ultrasonics Sonochemistry* **59** (2019) 104696. https://doi.org/10.1016/j.ultsonch.2019.104696

[70] G. Xia, N. Li, D. Li, R. Liu, C. Wang, Q. Li, X. Lu, Graphene/Fe_2O_3/SnO_2 ternary nanocomposites as a high-performance anode for lithium-ion batteries, *ACS applied materials & interfaces* **5** (2013) 8607-8614. https://doi.org/10.1021/am402124r

[71] M. Parashar, V. K. Shukla, R. Singh - Metal oxides nanoparticles via sol–gel method: a review on synthesis, characterization and applications *Journal of Materials Science: Materials* **31** (2020) 3729–3749. https://doi.org/10.1007/s10854-020-02994-8

[72] J. H. Yoon, J. S. Kim, Gas sensing properties of nano-crystalline SnO_2-CuO compounds, *Metals and Materials International* **16** (2010) 773-777. https://doi.org/10.1007/s12540-010-1012-9

[73] H. Kose, S. Dombaycıoglu, A. O. Aydın, H. Akbulut, Production and characterization of free-standing ZnO/SnO_2/MWCNT ternary nanocomposite Li-ion battery anode, *International Journal of Hydrogen Energy* **41** (2016) 9924-9932. https://doi.org/10.1016/j.ijhydene.2016.03.202

[74] H. Kose, S. Dombaycıoglu, A. O. Aydn, Graphene-based architectures of tin and zinc oxide nanocomposites for free-standing binder-free Li-ion anodes. *International Journal of Energy Research* **42** (2018) 4710-4718. https://doi.org/10.1002/er.4223

[75] P. Tyagi, A. Sharma, M. Tomar, V. Gupta, A comparative study of RGO-SnO_2 and MWCNT-SnO_2 nanocomposites based SO_2 gas sensors, *Sensors and Actuators B: Chemical* **248** (2017) 980-986. https://doi.org/10.1016/j.snb.2017.02.147

[76] X. Ding, L. Lyu, F. Wang, Y. Yang, J. Qiao, D. Xu, X. Zhang, Novel ternary Co_3O_4/CeO_2/CNTs composites for high-performance broadband electromagnetic wave absorption, *Journal of Alloys and Compounds* **864** (2021) 158141. https://doi.org/10.1016/j.jallcom.2020.158141

[77] N. Raghavan, S. Thangavel, G. Venugopal, Enhanced photocatalytic degradation of methylene blue by reduced graphene-oxide/titanium dioxide/zinc oxide ternary nanocomposites, *Materials Science in Semiconductor Processing* **30** (2015) 321-329. https://doi.org/10.1016/j.mssp.2014.09.019

[78] H. Lv, G. Ji, H. Zhang, Y. Du, Facile synthesis of a CNT@ Fe@SiO_2 ternary composite with enhanced microwave absorption performance, *RSC advances* **5** (2015) 76836-76843. http://doi.org/10.1039/C5RA11162E

[79] D. Chaudhary, S. Singh, V. D. Vankar, N. Khare, A ternary Ag/TiO_2/CNT photoanode for efficient photoelectrochemical water splitting under visible light irradiation, *International Journal of Hydrogen Energy* **42** (2016) 7826-7835. https://doi.org/10.1016/j.ijhydene.2016.12.036

[80] J. Wang, W. Bao, L. Ma, G. Tan, Y. Su, S. Chen, F. Wu, J. Lu, Scalable Preparation of Ternary Hierarchical Silicon Oxide–Nickel–Graphite Composites for Lithium-Ion Batteries, *ChemSusChem* **8** (2015) 4073-4080. https://doi.org/10.1002/cssc.201500674

[81] Ismail, Ternary CNTs@TiO_2/CoO Nanotube Composites: Improved Anode Materials for High Performance Lithium-Ion Batteries, Materials 2017, 10(6), 678 11-14 https://doi.org/10.3390/ma10060678

[82] L. Sun, Q. Deng, Y. Li, L. Deng, Y. Wang, X. Ren, P. Zhang, Solvothermal synthesis of ternary Cu_2O-CuO-RGO composites as anode materials for high performance lithium-ion batteries, *Electrochimica Acta* **222** (2016) 1650-1659. https://doi.org/10.1016/j.electacta.2016.11.155

[83] G. D. Varma, Synthesis of CuO-ZnO/rGO ternary composites for superior NO_2 gas sensor at room temperature, *Materials Research Express* **6** (2018) 035011. http://doi.org/10.1088/2053-1591/aaf34c

[84] K. Chaudhary, N. Shaheen, S. Zulfiqar, M.I. Sarwar, Binary WO_3-ZnO nanostructures supported rGO ternary nanocomposite for visible light driven photocatalytic degradation of methylene blue, *Synthetic Metals* **269** (2020) 116526. https://doi.org/10.1016/j.synthmet.2020.116526

[85] D. A. Reddy, R. Ma, T. K. Kim, Efficient photocatalytic degradation of methylene blue by heterostructured ZnO–RGO/RuO_2 nanocomposite under the simulated sunlight irradiation,

Ceramics international **41** (2015) 6999-7009. https://doi.org/10.1016/j.ceramint.2015.01.155

[86] Y. Zheng, Z. Liu, B. Liu, S. Wang, C. Xiong, Fabrication of cactus-like CNT/SiO_2/MoO_3 ternary composites for superior lithium storage, *Energy* **217** (2021) 119386. https://doi.org/10.1016/j.energy.2020.119386

[87] V. Perez-Luna, M. Cisneros, C. Bittencourt, I. Saucedo-Orozco, M. Quintana, Imaging carbon nanostructures' reactivity: a complementary strategy to define chemical structure, *Royal Society open science* **5** (2018) 180605. https://doi.org/10.1098/rsos.180605

[88] F. T. Johra, W. G. Jung, RGO–TiO_2–ZnO composites: synthesis, characterization, and application to photocatalysis, *Applied Catalysis A: General* **491** (2015) 52-57. https://doi.org/10.1016/j.apcata.2014.11.036

[89] C. Wang, J. Sun, Y. Sun, Z. Tan, X. Xu, Y. Fu, Z. Feng, J. Zhu, Fabrication of cubic Co_3O_4-hexagonal ZnO disk/rGO as a two-phase benzaldehyde sensor via a sequential nucleation strategy, *Sensors and Actuators B: Chemical* **330** (2021) 129384. https://doi.org/10.1016/j.snb.2020.129384

[90] N. Butterfield, P.M. Rowe, E. Stewart, D. Roesel, S. Neshyba, Quantitative three-dimensional ice roughness from scanning electron microscopy, *Journal of Geophysical Research: Atmospheres* 122 (2017) 3023-3041. https://doi.org/10.1002/2016JD026094

[91] H. Heidari, W. Van den Broek, S. Bals, Quantitative electron tomography: The effect of the three-dimensional point spread function, *Ultramicroscopy* **135** (2013) 1-5. https://doi.org/10.1016/j.ultramic.2013.06.005

[92] D. B. Williams, C. B. Carter, T*ransmission Electron Microscopy: Spectrometry,* David B. Williams and C. Barry Cart. IV. Plenum, 1996.

[93] K. T. Nam, D. W. Kim, P. J. Yoo, C. Y. Chiang, N. Meethong, Virus-enabled synthesis and assembly of nanowires for lithium-ion battery electrodes, *Science* **312** (2006) 885-888. http://doi.org/10.1126/science.112271

[94] W. Shaheen, M. F. Warsi, M. Shahid, M. A. Khan, M. Asghar, Z. Ali, M. Sarfraz, H. Anwar, M. Nadeem, I. Shakir, Carbon coated MoO_3 nanowires/ graphene oxide ternary nanocomposite for high-performance supercapacitors, *Electrochimica Acta* **219** (2016) 330-338. https://doi.org/10.1016/j.electacta.2016.09.069

[95] Y. Li, B. Tan, Y. Wu, Mesoporous Co_3O_4 nanowire arrays for lithium-ion batteries with high capacity and rate capability, *Nano letters* **8** (2008) 265-270. https://doi.org/10.1021/nl0725906

[96] C. Rodriguez-Quijada, K. Hamad-Schifferli, *Applications of Plasmonic Nanomaterials for Phototriggered Theranostics*, In Handbook of Nanomaterials for Cancer Theranostics, Elsevier (2018) 125-142. https://doi.org/10.1016/B978-0-12-813339-2.00005-0

[97] D.K. Denis, X. Sun, J. Zhang, Y. Wang, L. Hou, J. Li, and C. Yuan, Solid solution engineering of Co–Ni-based ternary molybdate nanorods toward hybrid supercapacitors and lithium-ion batteries as high-performance electrodes, *ACS Applied Energy Materials* **3** (2020) 3955-3965. https://doi.org/10.1021/acsaem.0c00353

[98] J. Guo, L. Chen, X. Zhang, H. Chen, Porous Co_3O_4 nanorods as anode for lithium-ion battery with excellent electrochemical performance, *Journal of Solid State Chemistry* **213** (2014) 193-197. https://doi.org/10.1016/j.jssc.2014.02.036

[99] Q. Wang, D. A. Zhang, Q. Wang, J. Sun, L. L. Xing, X. Y. Xue, High electrochemical performances of α-MoO_3@MnO_2 core-shell nanorods as lithium-ion battery anodes, *Electrochimica Acta* **146** (2014) 411-418. https://doi.org/10.1016/j.electacta.2014.09.020

[100] L. Zuniga, G. Gonzalez, R. Orrostieta Chavez, J. C. Myers, T. P. Lodge & M. Alcoutlabi Centrifugally Spun α-Fe_2O_3/TiO_2/Carbon Composite Fibers as Anode Materials for Lithium-Ion Batteries, *Applied Sciences* **9** (2019) 4032. https://doi.org/10.3390/app9194032

[101] X. Jin, T.H. Gu, K. G. Lee, M. J. Kim, M. S. Islam, Unique advantages of 2D inorganic nanosheets in exploring high-performance electrocatalysts: synthesis, application, and perspective, *Coordination Chemistry Reviews* **415** (2020) 213280. https://doi.org/10.1016/j.ccr.2020.213280

[102] S. Wu, G. Fu, W. Lv, J. Wei, W. Chen, H. Yi, M. Gu, X. Bai, L. Zhu, C. Tan and Y.A. Liang, single-step hydrothermal route to 3D hierarchical Cu_2O/CuO/rGO nanosheets as high-performance anode of lithium-ion batteries, *Small* 14 (2018) 1702667. https://doi.org/10.1002/smll.201702667

[103] Q. Wei, J. Sun, P. Song, Z. Yang, Q. Wang, Synthesis of reduced graphene oxide/SnO_2 nanosheets/Au nanoparticles ternary composites with enhanced formaldehyde sensing performance, *Physica E: Low-dimensional Systems and Nanostructures* **118** (2020) 113953. https://doi.org/10.1016/j.physe.2020.113953

[104] Z. Wang, J. Mu, Y. Li, J. Chen, L. Zhang, D. Li, Preparation and lithium storage properties of NiO-SnO_2/graphene nanosheet ternary composites, *Journal of Alloys and Compounds* **695** (2017) 2909-2915. https://doi.org/10.1016/j.jallcom.2016.11.386

[105] Y. Feng, K. Wu, J. Ke, Z. Guo, X. Deng, C. Bai, Y. Sun, Synthesis of ternary SnO_2–MoO_3–C composite with nanosheet structure as high-capacity, high-rate and long-lifetime anode for lithium-ion batteries, *Ceramics International* **47** (2021) 9303-9309. https://doi.org/10.1016/j.ceramint.2020.12.057

[106] R. B. Anjaneyulu, B. S. Mohan, G. P. Naidu, R. Muralikrishna, Visible light enhanced photocatalytic degradation of methylene blue by ternary nanocomposite, MoO_3/Fe_2O_3/rGO. *Journal of Asian Ceramic Societies* 6 (2018) 183-195. https://doi.org/10.1080/21870764.2018.1479011

[107] H. Xiao, S. Yao, F. Qu, X. Zhang, X. Wu, Electrochemical energy storage performance of heterostructured SnO_2@ MnO_2 nanoflakes, *Ceramics International* **43** (2017)1688-1694. https://doi.org/10.1016/j.ceramint.2016.08.064

[108] K. Palanisamy, J. H. Um, M. Jeong, W. S. Yoon, Porous V_2O_5/RGO/CNT hierarchical architecture as a cathode material: Emphasis on the contribution of surface lithium storage, *Scientific reports* **6** (2016) 1-12. https://doi.org/10.1038/srep31275

[109] R. Li, W. Xiao, C. Miao, R. Fang, Z. Wang, M. Zhang, Sphere-like SnO_2/TiO_2 composites as high-performance anodes for lithium-ion batteries, *Ceramics International* **45** (2019) 13530-13535. https://doi.org/10.1016/j.ceramint.2019.04.059

[110] M. H. Kim, Y. C. Kang, Electrochemical properties of spherical hollow SnO_2-TiO_2-C composite powders prepared by spray pyrolysis, *International Journal of Electrochemical Science* **8** (2013) 3676-3686.

[111] D. Liu, X Wang, X Wang, W. Tian, Y. Bando, D. Golberg, Co_3O_4 nanocages with highly exposed {110} facets for high-performance lithium storage, *Scientific reports* **3** (2013) 1-6. https://doi.org/10.1038/srep02543

[112] B. Wang, X. Y. Lu, K. Y. Wong, Y. Tang, Facile solvothermal synthesis and superior lithium storage capability of Co_3O_4 nanoflowers with multi-scale dimensions, *Materials Chemistry Frontiers* **1** (2017) 468-476. http://doi.org/10.1039/C6QM00114A

[113] J. Chen, L. Yang, S. Fang, S. Hirano, K. Tachibana, Synthesis of hierarchical mesoporous nest-like $Li_4Ti_5O_{12}$ for high-rate lithium-ion batteries, *Journal of Power sources* **200** (2012) 59-66. https://doi.org/10.1016/j.jpowsour.2011.10.052

[114] W. W. Lee, J. M. Lee, Novel synthesis of high-performance anode materials for lithium-ion batteries (LIBs), *Materials Chemistry A* **2** (6) (2014) 1589-626**.** https://doi.org/10.1039/C3TA12830J

[115] Z. Yang, J. Zhang, M. C. W. Kintner-Meyer, X. Lu, D. Choi, J. P. Lemmon, J. Liu, Electrochemical energy storage for green grid, *Chemical reviews* 111 (2011) 3577-3613. https://doi.org/10.1021/cr100290v

[116] F. Zhan, B. Geng, Y. Guo, Porous Co_3O_4 nanosheets with extraordinarily high discharge capacity for lithium batteries, *Chemistry–A European Journal* 15 (2009) 6169-6174. https://doi.org/10.1002/chem.200802561

[117] N.T. Aristote, K. Zou, A. Di, W. Deng, B. Wang, X. Deng, X. Ji, Methods of improving the initial Coulombic efficiency and rate performance of both anode and cathode materials for sodium-ion batteries, *Chinese Chemical Letters* **33** (2022) 730-742. https://doi.org/10.1016/j.cclet.2021.08.049

[118] J. Zhu, Z. Lu, M. O. Oo, H. H. Hng, J. Ma, H. Zhang, Q. Yan, Synergetic approach to achieve enhanced lithium-ion storage performance in ternary phased SnO_2–Fe_2O_3/rGO composite nanostructures, *Journal of Materials Chemistry* **21** (2011) 12770-12776. https://doi.org/10.1039/C1JM12447A

[119] Y. Wang, H. Zhang, R. Hu, J. Liu, T. van Ree, H. Wang, L. Yang, and M. Zhu, Fe_3O_4/SnO_2/rGO ternary composite as a high-performance anode material for lithium-ion batteries, *Journal of Alloys and Compounds* **693** (2017) 1174-1179. https://doi.org/10.1016/j.jallcom.2016.10.082

[120] W. Wu, Y. Zhao, J. Li, C. Wu, L. Guan, A ternary phased SnO_2-Fe_2O_3/SWCNTs nanocomposite as a high-performance anode material for lithium-ion batteries, *Journal of energy chemistry* **23** (2014) 376-382. https://doi.org/10.1016/S2095-4956(14)60160-1

[121] B. N. Joshi, S. An, Y. I. Kim, E.P. Samuel, K. Y. Song, I. W. Seong, S. S. Al-Deyab, M. T. Swihart, W. Y. Yoon and S. S. Yoon, Flexible freestanding Fe_2O_3-SnO_x-carbon nanofiber composites for Li ion battery anodes, *Journal of Alloys and Compounds* **700** (2017) 259-266. https://doi.org/10.1016/j.jallcom.2017.01.057

[122] H. Kose, S. Dombaycioglu, A. O. Aydin, Production and characterization of free-standing ZnO/SnO_2/MWCNT ternary nanocomposite Li-ion battery anode, *International Journal of Hydrogen Energy* **41** (2016) 9924-9932. https://doi.org/10.1016/j.ijhydene.2016.03.202

[123] Z. Jiao, R. Gao, H. Tao, S. Yuan, L. Xu, S. Xia, H. Zhang, Intergrown SnO_2–TiO_2@ graphene ternary composite as high-performance lithium-ion battery anodes, *Journal of Nanoparticle Research* **18** (2016) 1-12. https://doi.org/10.1007/s11051-016-3617-5

[124] S. Li, M. Ling, J. Qiu, J. Han, S. Zhang, Anchoring ultra-fine TiO_2–SnO_2 solid solution particles onto graphene by one-pot ball-milling for long-life lithium-ion batteries, *Journal of Materials Chemistry A* **3** (2015) 9700-9706. https://doi.org/10.1039/C5TA01350J

[125] S. Han, J. Jiang, Y. Huang, Y. Tang, J. Cao, D. Wu, X. Feng, Hierarchical TiO_2–SnO_2–graphene aerogels for enhanced lithium storage, *Physical Chemistry Chemical Physics* 17 (2015) 1580-1584. https://doi.org/10.1039/C4CP04887C

[126] X. Jiang, X. Yang, Y. Zhu, K. Fan, P. Zhao, C. Li, Designed synthesis of graphene–TiO_2–SnO_2 ternary nanocomposites as lithium-ion anode materials, *New Journal of Chemistry* 37 (2013) 3671-3678. https://doi.org/10.1039/C3NJ00797A

[127] Y. Tang, D. Wu, S. Chen, F. Zhang, J. Jia, X Feng, Highly reversible and ultra-fast lithium storage in mesoporous graphene-based TiO_2/SnO_2 hybrid nanosheets, *Energy & Environmental Science* 6 (2013) 2447-2451. https://doi.org/10.1039/C3EE40759D

[128] S. Li, M. Ling, J. Qiu, J. Han, S. Zhang, Anchoring ultra-fine TiO_2–SnO_2 solid solution particles onto graphene by one-pot ball-milling for long-life lithium-ion batteries, *Journal of Materials Chemistry A* 3 (2015) 9700-9706. http://doi.org/10.1039/c5ta01350j

[129] D. Bao, Q. Tian, Interconnected quasi-nanospheres of SnO_2/TiO_2/C with gap spaces for improved lithium storage, *Materials Letters* 229 (2018) 48-52. https://doi.org/10.1016/j.matlet.2018.06.062

[130] V.A. Agubra, L. Zuniga, D. Flores, H. Campos, J. Villarreal, A comparative study on the performance of binary SnO_2/NiO/C and Sn/C composite nanofibers as alternative anode materials for lithium-ion batteries, *Electrochimica Acta* **224** (2017) 608-621. https://doi.org/10.1016/j.electacta.2016.12.054

[131] Y. Sun, Y. Feng, J. Ke, X. Deng, W. Li, Z. Guo, M. He, SnO_2-Co_3O_4-graphite nanosheets with stable structure, high reversible capacity, and long life as anode material for lithium-ion batteries, *Ionics* **27** (2021) 4167-4175. https://doi.org/10.1007/s11581-021-04192-w

[132] Y. Wang, W. Guo, Y. Yang, Y. Yu, Q. Li, D. Wang, F. Zhang, Rational design of SnO_2@C@ MnO_2 hierarchical hollow hybrid nanospheres for a Li-ion battery anode with enhanced performances, *Electrochimica Acta* **262** (2018) 1-8. https://doi.org/10.1016/j.electacta.2017.12.181

[133] W. Li, X. Deng, Y. Feng, D. Xiong, M. He, Synthesis of SnO_2@ MnO_2@ graphite nanosheet with high reversibility and stable structure as a high-performance anode material for lithium-ion batteries, *Ceramics International* **47** (2021) 33405-33412. https://doi.org/10.1016/j.ceramint.2021.08.247

[134] J. Zhang, P. Gu, J. Xu, H. Xue, H. Pang, High performance of electrochemical lithium storage batteries: ZnO-based nanomaterials for lithium-ion and lithium–sulfur batteries, *Nanoscale* **8** (2016) 18578-18595. https://doi.org/10.1039/C6NR07207K

[135] G. Yuan, G. Wang, H. Wang, J. Bai, Synthesis and electrochemical investigation of radial ZnO microparticles as anode materials for lithium-ion batteries, *Ionics* **21** (2015) 365-371. https://doi.org/10.1007/s11581-014-1188-y

[136] C. T. Hsieh, C. Y. Lin, Y. F. Chen, J. S. Lin, Synthesis of ZnO@ Graphene composites as anode materials for lithium-ion batteries, *Electrochimica Acta* **111** (2013) 359-365. https://doi.org/10.1016/j.electacta.2013.07.197

[137] S. Lu, H. Wang, J. Zhou, X. Wu, W. Qin, Atomic layer deposition of ZnO on carbon black as nanostructured anode materials for high-performance lithium-ion batteries, *Nanoscale* **9** (2017) 1184-1192. https://doi.org/10.1039/C6NR07868K

[138] D. Bresser, F. Mueller, M. Fiedler, S. Krueger, R. Kloepsch, D. Baither, M. Winter, E. Paillard, S. Passerini, Transition-metal-doped zinc oxide nanoparticles as a new lithium-ion anode material, *Chemistry of Materials* **25** (2013) 4977-4985. https://doi.org/10.1021/cm403443t

[139] Y. Huang, X. Chen, K. Zhang, X. Feng, Preparation of graphene supported flower-like porous 3D ZnO–NiO ternary composites for high-capacity anode materials for Li-ion batteries, *Ceramics International* 41 (2015) 13532-13540. https://doi.org/10.1016/j.ceramint.2015.07.147

[140] X. He, Y. Hu, R. Chen, Z. Shen, K. Wu, Z. Cheng, P. Pan, Foldable uniform GeO_x/ZnO/C composite nanofibers as a high-capacity anode material for flexible lithium ion batteries, *Chemical Engineering Journal* **360** (2019) 1020-1029. https://doi.org/10.1016/j.cej.2018.10.163

[141] Y. Ma, D. Geiger, U. Kaiser, H. Zhang, G. T. Kim, T. Diemant, R. J. Behm, A. Varzi, S. Passerini, ZnO/$ZnFe_2O_4$/N-doped C micro-polyhedrons with hierarchical hollow structure as high-performance anodes for lithium-ion batteries, *Nano Energy* 42 (2017) 341-352. https://doi.org/10.1016/j.nanoen.2017.11.030

[142] J. Zhao, H. Zhou, M. Jin, P. Chen, S. Chen, X. Liu, ZnO/TiO_2/C nanofibers by electrospinning for high-performance lithium storage, *Journal of Materials Science* 56 (2021) 2497-2505. https://doi.org/10.1007/s10853-020-05363-2

[143] X. Cheng, Y. Li, L. Sang, J. Ma, H. Shi, X. Liu, J. Lu, Boosting the electrochemical performance of MoO_3 anode for long-life lithium-ion batteries: Dominated by an ultrathin TiO_2 passivation layer, *Electrochimica Acta* 269 (2018): 241-249. https://doi.org/10.1016/j.electacta.2018.03.009

[144] T. Anwar, L. Wang, L. Jiaoyang, W. Chen, R. U. R. Sagar, L. Tongxiang, Lithium storage study on MoO_3-grafted TiO_2 nanotube arrays, *Applied NanoScience* 6 (2016) 1149-1157. https://doi.org/10.1007/s13204-016-0526-y

[145] X. Deng, M. Zhu, J. Ke, W. Li, Y. Feng, D. Xiong, M. He, SnO_2-MoO_3 nanoparticles anchored in carbon nanotubes as a large-capacity, high-rate, and long-lifetime anode for lithium-ion batteries, *Ceramics International* **47** (2021) 27022-27031. https://doi.org/10.1016/j.ceramint.2021.06.115

[146] L. Cao, Y. Li, J. Wu, W. Li, J. Huang, Y. Feng, C. Yao, J. Li, Facile synthesis of carbon coated MoO_3 nanorods decorated with WO_2 nanoparticles as stable anodes for lithium-ion batteries, *Journal of Alloys and Compounds* **744** (2018) 672-678. https://doi.org/10.1016/j.jallcom.2018.02.112

[147] Y. Teng, H. Liu, D. Liu, Y. Chen, A hierarchically nanostructured composite of MoO_3-NiO/graphene for high-performance lithium-ion batteries, *Journal of Electrochemical Energy Conversion and Storage* **18** (2021) 031003. https://doi.org/10.1115/1.4048492

[148] M. T. McDowell, S. W. Lee, W. D. Nix, Y. Cui, 25th Understanding the Lithiation of Silicon and Other Alloying Anodes for Lithium-Ion Batterie s, *Advance Materials* **25** (2013) 4966-4984. https://doi.org/10.1002/adma.201301795

[149] J. K. Lee, C. Oh, N. Kim, J. Hwang, Y. Sun, Rational design of silicon-based composites for high-energy storage devices, *Journal of Materials Chemistry* A **4**(15) (2016) 5366-5384. http://doi.org/10.1039/C6TA00265J

[150] Z. Gu, W. Li, Y. Chen, X. Xia & H. Liu, Synthesis of the microspherical structure of ternary SiO_x@SnO_2@C by a hydrothermal method as the anode for high-performance lithium-ion batteries, *Sustainable Energy & Fuels* **4** (2020) 2333-2341. https://doi.org/10.1039/D0SE00053A

[151] Z. Hu, H. Cui, J. Li, G. Lei & Z. Li, Constructing three-dimensional Li-transport channels within the Fe_3O_4@SiO_2@RGO composite to improve its electrochemical performance in Li-ion batteries, *Ceramics International* **46** (2020) 18868- 18877. https://doi.org/10.1016/j.ceramint.2020.04.207

[152] F. Tan, H. Guo, Z. Wang, X. Niu, X. Li, G. Yan, Q. Hu, Electrospinning-enabled SiO_x@TiO_2/C fibers as anode materials for lithium-ion batteries, *Journal of Alloys and Compounds* **888** (2021) 161635. https://doi.org/10.1016/j.ceramint.2020.04.207

[153] Y. Jiang, S. Chen, D. Mu, Z. Zhao, C. Li, Z. Din, F. Wu, Flexible TiO_2 /SiO_2 /C Film Anodes for Lithium-Ion Batteries, *ChemSusChem* **11** (2018) 2040–2044. https://doi.org/10.1002/cssc.201800560

[154] J. Y. Liao, D. Higgins, G. Lui, V. Chabot, X. Xiao, Z. Chen, Multifunctional TiO_2–C/MnO_2 core–double-shell nanowire arrays as high-performance 3D electrodes for lithium-ion batteries, *Nano letters* **13** (2013) 5467-5473. https://doi.org/10.1021/nl4030159

[155] V. Etacheri, C. N. Hong, J. Tang, V. G. Pol, Cobalt nanoparticles chemically bonded to porous carbon nanosheets: a stable high-capacity anode for fast-charging lithium-ion batteries, *ACS applied materials & interfaces* **10** (2018) 4652-4661. https://doi.org/10.1021/acsami.7b15915

[156] Y. Lu, J. Tu, C. Gu, X. Wang, S. X. Mao, In situ growth and electrochemical characterization versus lithium of a core/shell-structured Ni_2P@C nanocomposite synthesized by a facile organic-phase strategy, *Journal of Materials Chemistry* **21** (2011) 17988-17997. https://doi.org/10.1039/C1JM13171K

[157] L. Ji, Z. Lin, M. Alcoutlabi, X. Zhang, Recent developments in nanostructured anode materials for rechargeable lithium-ion batteries, *Energy & Environmental Science* **4** (2011) 2682-2699. https://doi.org/10.1039/C0EE00699H

[158] L. Zuniga, V. Agubra, D. Flores, H. Campos, J. Villareal, Multichannel hollow structure for improved electrochemical performance of TiO_2/Carbon composite nanofibers as anodes for lithium-ion batteries, *Journal of Alloys and Compounds* **686** (2016) 733-743. https://doi.org/10.1016/j.jallcom.2016.06.089

[159] C. Wang, Q. Li, F. Wang, G. Xia, R. Liu, D. Li, N. Li, Morphology-dependent performance of CuO anodes via facile and controllable synthesis for lithium-ion batteries, *ACS applied materials & interfaces* **6** (2014) 1243-1250. https://doi.org/10.1021/am405061c

[160] L. Zuniga, G. Gonzalez, R. Orrostieta Chavez, J. C. Myers, Centrifugally spun α-Fe_2O_3/TiO_2/carbon composite fibers as anode materials for lithium-ion batteries, *Applied Sciences* **9** (2019) 4032. https://doi.org/10.3390/app9194032

[161] K. Kaprans, J. Mateuss, A. Dorondo, G. Bajars, Electrophoretically deposited α-Fe_2O_3 and TiO_2 composite anchored on rGO with excellent cycle performance as anode for lithium-ion batteries, *Solid State Ionics* **319** (2018) 1-6. https://doi.org/10.1016/j.ssi.2018.01.042

[162] F. Wang, H. Yuan, J. Huang, A bio-inspired nanofibrous Co_3O_4/TiO_2/carbon composite as high-performance anodic material for lithium-ion batteries, *Journal of Alloys and Compounds* **819** (2020) 153375. https://doi.org/10.1016/j.jallcom.2019.153375

[163] H. Zhang, Y.F. Wang, W. L. Liu, F. G. Kong, M. M. Ren, Designed synthesis of CoO/CuO/rGO ternary nanocomposites as high-performance anodes for lithium-ion batteries, *Jom* **70** (2018) 1793-1799. https://doi.org/10.1007/s11837-018-2801-8

[164] J. B. Wu, R. Q. Guo, X. H. Huang, Y. Lin, Ternary core/shell structure of Co_3O_4/NiO/C nanowire arrays as high-performance anode material for Li-ion battery, *Journal of Power Sources*, **248** (2014) 115-121. https://doi.org/10.1016/j.jpowsour.2013.09.040

[165] S. Balamurugan, N. Naresh, I, Prakash, N. Satyanarayana, Capacity fading mechanism of Li_2O loaded $NiFe_2O_4$/SiO_2 aerogel anode for Lithium-ion battery: Ex-situ XPS analysis, *Applied Surface Science* **535** (2020) 147677. https://doi.org/10.1016/j.apsusc.2020.147677

[166] B. Ziv, V. Borgel, D. Aurbach, J. -H. Kim, X. Xiao & B. R. Powell, Investigation of the Reasons for Capacity Fading in Li-Ion Battery Cells, *Journal of The Electrochemical Society* **161** (2014) A1672–A1680. http://doi.org/10.1149/2.0731410jes

[167] H. -R. Kim, S. -G. Woo, J. -H. Kim, W. Cho & Y. -J. Kim Capacity fading behaviour of Ni-rich layered cathode materials in Li-ion full cells, *Journal of Electroanalytical Chemistry* **782** (2016) 168–173. https://doi.org/10.1016/j.jelechem.2016.10.032